Desalination 622 (2026) 119622

Contents lists available at ScienceDirect

Desalination

journal homepage: www.elsevier.com/locate/desal

Early detection and control of $CaCO_3$ scaling in closed-circuit reverse osmosis under antiscalant-free conditions

Martin Futterlieb [a,*], Stefan Panglisch [a,b,c,d]

[a] University of Duisburg-Essen, Lotharstr. 1, 47057 Duisburg, Germany
[b] IWW Water Center, Moritzstraße 26, 45476 Mülheim an der Ruhr, Germany
[c] Center for Water and Environmental Research (ZWU), Universitätsstraße 2, 45141 Essen, Germany
[d] DGMT German Society of Membrane Technology, Geschäftsstelle ZWU, Universitätsstraße 2, 45141 Essen, Germany

HIGHLIGHTS

- Concentrate-pH indicated incipient $CaCO_3$ scaling, the earliest and most reliable.
- Early detection enables long-term anti-scalant-free operation.
- Inherent flushing removes fouling and scaling layers.
- Short time at high saturation promotes formation of mineral precursors.
- Higher solubility of precursors enables dissolution by inherent flushing.

GRAPHICAL ABSTRACT

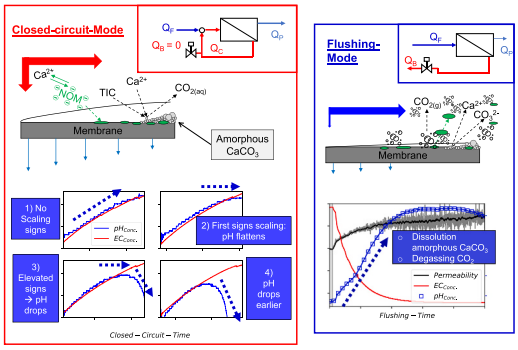

ARTICLE INFO

Keywords:
Closed-circuit reverse osmosis
$CaCO_3$ scaling
Scaling mitigation
Early scaling detection
Antiscalant-free operation

ABSTRACT

Recently, discontinuous operation modes, such as closed-circuit reverse osmosis (CCRO), have gained importance. CCRO allegedly offers various benefits, such as increased scaling resistance. However, there is limited understanding of how CCRO operation affects membrane performance parameters. Beyond that, the alleged scaling resistance is poorly understood and, in some instances, even subject to contradictory findings. In addition, scaling detection in CCRO remains largely unexplored. To investigate these open questions, we operated a semi-technical plant with a spiral-wound element fed with a real water matrix inducing $CaCO_3$ scaling and organic fouling without antiscalant dosing. Under non-scaling conditions rejection increases within a closed-circuit, correlating with rising concentrate pH. Monitoring concentrate pH proves effective for detecting $CaCO_3$ scaling, as it is first indicated by the flattening of the pH curve and later by a decreasing pH during closed-circuit operation. This method prevented membrane scaling in long-term experiments (>54 days). Process inherent flushing partially removes organic fouling. Moreover, flushing triggers the dissolving of $CaCO_3$ deposits, likely due to the relatively short duration under high saturation. This leads to the formation of calcite precursors like amorphous $CaCO_3$, as supported by water chemistry simulations. This research extends, thus, current knowledge on anti-scaling mechanisms in discontinuous operation and opens up a new direction for antiscalant-free desalination.

* Corresponding author.
E-mail address: martin.futterlieb@uni-due.de (M. Futterlieb).

https://doi.org/10.1016/j.desal.2025.119622
Received 3 September 2025; Received in revised form 26 October 2025; Accepted 9 November 2025
Available online 17 November 2025

1. Introduction

In the last two decades, discontinuous semi-batch and batch-operation of reverse osmosis (RO) and nanofiltration (NF) processes has gained increasing attention due to several proposed advantages over conventional continuous flow RO (CoFRO) [1–3]. Currently, the most relevant process in practice is semi-batch operation known as closed-circuit RO (CCRO). This process was first commercialized by Desalitech [4], a company that later became part of DuPont [5]. CCRO is a discontinuous process consisting of two alternating modes, the closed-circuit-mode (CC) and the flushing-mode [3]. In the CC-mode, the entire concentrate is recirculated until a desired recovery is reached and flushing is initiated, in which the concentrate is discharged and replenished with feedwater [3,6–8], see Fig. 1 a. Thereby, the recovery is a function of the time rather than the implemented elements and stages in series as in conventional multi-stage CoFRO [3,6]. This allows high-recovery operation with a single-stage configuration, and the inherent concentrate recirculation minimizes hydraulic limitations, such as minimum concentrate-flow restrictions [9]. Batch and semi-batch processes including CCRO were studied extensively regarding potential energy benefits in desalination [1,3,4,6–8,10,11]. Moreover, batch and semi-batch operations are allegedly less prone to scaling [1,9,12–15].

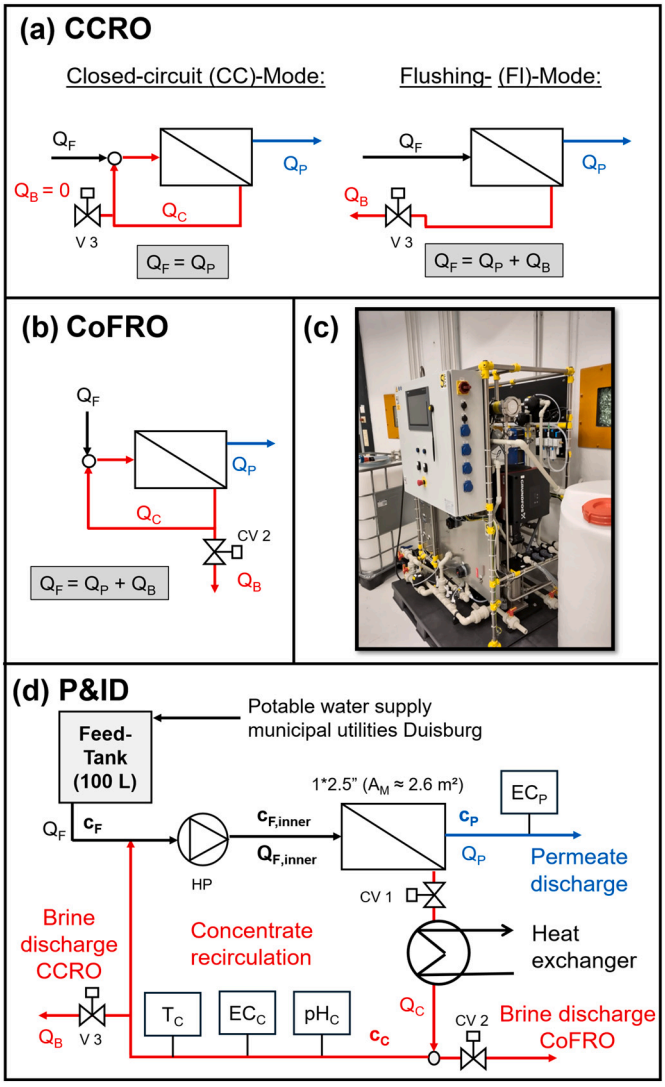

Fig. 1. Semi-technical plant; possible modes of operation as CCRO (a) and continuous RO (CoFRO) (b); c) picture of plant and d) simplified P&ID.

Although antiscalants are effective in mitigating membrane scaling [16], their application is associated with several drawbacks. First, the discharge of brines containing antiscalants presents environmental concerns [17]. Additionally, traces of antiscalants can permeate through the membrane [18,19]. The presence of antiscalants in the permeate is problematic, as it may lead to the formation of harmful disinfection byproducts [19]. Enhancing scaling resistance by implementing discontinuous operation may thus reduce, or even eliminate the necessity for antiscalants.

However, possible reasons for the alleged higher scaling resistance in batch and semi-batch processes are poorly understood and partially based on theoretical studies [9,13]. Moreover, higher susceptibility towards scaling in semi-batch operation is reported, too [20]. Furthermore, practical studies reporting scaling-resistance are typically limited to short-term experiments, whereas long-term experience regarding potential benefits with respect to fouling and scaling is lacking [14,15]. In general, the discontinuous operation has several aspects, which might counter the occurrence of scaling, namely, inherent periodic flushing, osmotic backwash, salinity cycling, and, depending on the configuration, also flow reversal [14]. Salinity cycling arises from the interplay between CC- and flushing-mode. Within CC-mode, the salinity continuously rises until flushing restores the initial salinity, and subsequently, a new cycle starts. The membrane is, thus, only temporary in contact with supersaturated solutions. Warsinger et al. [13] suggested that thereby the nucleation induction time is undershot, preventing the precipitation of sparingly soluble salts. Already two decades ago, this approach was demonstrated using periodic flow reversal to reset the nucleation induction time successfully [21]. The benefits of (forward) flushing are well known for conventional RO operation [22], however, the inherent periodic occurrence of flushing in discontinuous operation and its possible benefits are less studied [14]. Gu et al. [23] observed higher scaling resistance than initially expected in CCRO operation and proposed scaling mitigation due to frequent flushing. In our previous study [24], we demonstrated that forward flushing in CoFRO (partially) restored the permeability, and we suspected that the dissolution of $CaCO_3$ precipitates was the cause. We therefore concluded that CCRO operation could be advantageous, as the inherent flushing could dissolve the limescale deposits that had formed. However, possible dissolution mechanisms remained unclear, since the feedwater was already supersaturated for calcite [24].

Although there is extended literature on early-scaling detection, e.g., by concentrate- observation [24,25], optical fibers [26], surface imaging [27–32], or Raman spectroscopy [33–37], to the best of our knowledge, only the recent study of Schwiebert et al. [25] investigated early detection in batch-operation. The authors successfully applied concentrate turbidity monitoring to counter gypsum and $CaCO_3$ scaling treating a synthetic solution mimicking an agricultural runoff. The study demonstrated that employing a turbidity-based approach enabled increased recovery in the absence of antiscalants [25]. This, in turn, facilitated effective brine treatment, for example, allowing the reclamation of gypsum for soil amendment or the pursuit of even higher recovery rates [25].

Beyond that, our earlier study [24], showed that, in the selected measurement and experimental setup, monitoring the concentrate pH value indicates the onset of $CaCO_3$ scaling early, more reliably and more significantly than all other parameters investigated (EC, turbidity, permeability, salt-rejection, pressure-drop). For this reason, we have suggested that this early detection method of scaling is highly applicable to discontinuous operating processes such as CCRO. A decrease in pH can be attributed to CO_2 release, which occurs during $CaCO_3$ precipitation [24,38]. Consequently, an increasing pH is associated to $CaCO_3$ dissolution.

In the present study we investigated open questions regarding CCRO, namely the challenges of non-steady operation, options to detect and mitigate $CaCO_3$ scaling on an early stage, and the possible benefits of inherent (feed) flushing to counter both fouling and scaling. In contrast

to prevailing studies on scaling in batch and semi-batch operation, we utilized a semi-technical plant equipped with a pressure vessel and a spiral-wound element, rather than lab-scale setups, to investigate early detection of scaling. In addition, long-term tests were carried out instead of short-term tests, and a real water matrix saturated with respect to calcite was used instead of synthetic feed solutions. This approach enabled observation of real operational conditions, including overlapping fouling and scaling.

Initially, CCRO operation was studied under non-scaling conditions to better understand the complex interactions of standard membrane performance parameters, such as rejection, in discontinuous operation (chapter 3.1). Subsequently, various parameters were compared in terms of their suitability for detecting incipient $CaCO_3$-scaling (chapter 3.2). Beyond that, the proposed anti-scaling mechanism, flushing, was studied, particularly whether the inherent feed flushing can actually lead to the dissolution of scale deposits that have already formed (chapter 3.3). Finally, the feasibility of long-term operations without antiscalant dosage at high recoveries was investigated, using a novel approach of pH-control to detect and mitigate incipient $CaCO_3$-scaling (chapter 3.4).

2. Material and methods

2.1. Feedwater

The feedwater for all experiments except Exp. 2 (see Table 2) was Duisburg tap water from the supply area north [39]. Table 1 summarizes the number of samples, average, maximum, and minimum values for selected parameters. The water induces $CaCO_3$-scaling ($SI_{Calcite} = 0.38$ and $SI_{Aragonite} = 0.24$). For this feedwater, the specific ultraviolet absorbance (SUVA in $L/(mgC*m)$), calculated as absorbance at 254 nm divided by the total organic carbon (TOC), indicates a proportion of humic substances and other natural organic matter (NOM) [40]. The water matrix being investigated is of a similar quality to typical pretreated feed for inland desalination plants (e.g., as applied in Germany for softening). Although the hardness of the feed can be classified as moderate [39], high recoveries can lead to more challenging scaling conditions. Moreover, the relatively high DOC reflects typical practical issues of overlapping fouling and scaling.

In Exp. 2, besides tap water, a 10 mM Na_2CO_3 (Riedel-de Haen, minimum assay: 99.8 %) solution was prepared using demineralized water (EC < 10 µS/cm). Moreover, in Exp. 3.2, the pH of tap water was gradually decreased using 1 M HCl and increased stepwise with 1 M NaOH to investigate the effect of the pH on the rejection.

2.2. Semi-technical plant

Fig. 1 depicts the semi-technical plant (c), the possible modes of operation (a and b), and a simplified piping and instrumentation diagram (d). The plant can be operated as CCRO (a) or conventional continuous CoFRO (b). In CCRO operation, one CC-mode and the subsequent flushing-mode are considered one cycle. In CC-mode, the brine discharge valve (V3) is closed. Thus, the entire concentrate is recirculated, while the incoming feed (Q_F) equals the produced permeate (Q_P). In flushing-mode, the discharge valve (V3) opens, and the concentrated brine is replenished by feedwater. Both brine and permeate are discharged into a container that is open to the atmosphere. In contrast to typical CCRO plants, our configuration uses an external rather than an internal recirculation and operates consequently without a recirculation pump. This configuration was chosen because we demonstrated comparable results for scaling and fouling when using internal or external recirculation in our previous study [24], and because the external configuration allows for easy integration of online monitoring of concentrate quality parameters. The plant can further operate as a CoFRO with concentrate recirculation. Unlike in CCRO, brine is continuously discharged through the control valve (CV2) during CoFRO, i.e., feed and bleed operation. The plant is fully automated and was constructed by the company SIMA- tec GmbH (Schwalmtal, Germany). It has a standard 2.5-in. (“) diameter and 40” length pressure vessel, which is equipped with one spiral wound elements (≈2.6 m^2 active membrane surface). The plant monitors online pressure (feed, concentrate, permeate), flow rate (permeate, concentrate), electrical conductivity (EC) (permeate, concentrate), pH (permeate and concentrate), and temperature. More details regarding the plant and the implemented online measurements can be found in the Supplementary Information of our previous study [24].

Table 1
Feed composition of tap water experiments.

Parameter	Unit	n	Average	Min	Max
Temperature	°C	31	16.3	14.8	21.3
pH	–	36	7.86	7.65	8.01
Conductivity	µS/cm	37	504.9	422.0	583.0
TDS		18	357	329	388
Sodium		35	19.2	17.2	22.6
Calcium		35	74.2	67.3	84.6
Magnesium	mg/L	35	4.6	3.7	5.2
Chloride		18	24.3	22.1	25.6
Sulfate		18	43.7	41.6	46.7
Hydrogen-carbonate		26	178.3	164.9	190.4
Nitrate as N	mgN/L	18	2.85	2.78	2.96
TOC ≈ DOC	mgC/L	26	3.2	2.9	4.0
SAC	(1/m)	13	9.2	7.9	11.8
SUVA	L/(mgC*m)	12	2.7	2.1	3.0
$SI_{Calcite}$	(−)		**0.38**		

2.3. Summary of experiments and experimental procedure

Table 2 lists the experiments. In the case of CCRO operation, the flux and the recovery refer to the CC-mode. All experiments were controlled by the desired flux (constant flux operation) and concentrate flow rate.

Before the experiments, the membranes were compacted for at least one day. Permeability and EC-rejection were continuously tracked to evaluate the state of compaction and to determine the starting conditions. After scaling experiments, the set-up was cleaned following an acid-base-acid cleaning protocol, with citric acid, NaOH and HCl,

Table 2
Summary of all experiments and respective operation mode.

Experiment ID	Operational parameter			Membrane	Feed
	Mode of operation	Flux (LMH)	Recovery (%)[a]		
Exp. 0	CoFRO	20	70	BW30 2540 (DuPont) 2.6 m^2 [41]	Tap water
Exp. 1		25	84 %		
Exp. 2	CCRO	40	76 %		Tap water and 10 mM Na_2CO_3 solution
Exp. 3.1		30, 10, 20	71, 44, 62		Tap water
Exp. 3.2	CoFRO	20	≈7 %		Tap water + HCl, NaOH
Exp. 4	CCRO	25	Increased the recovery from 82 to 85 to 87 %		
Exp. 5	CCRO	30	93.5 %		Tap water
Exp. 6	CCRO	36.5	Varied: 76 to 87 %	XLE Pro 2540 (DuPont) 2.6 m^2 [42]	

[a] In CCRO the recovery shown refers to the recovery in the closed-circuit mode (ϕ_{CC}).

respectively, following typical membrane supplier's guidelines [22]. After each step, the permeability and EC-rejection were checked and if necessary, cleaning continued, or membranes were exchanged. Anti-scalants were not used in any experiment.

2.4. Lab analysis

Cations and anions were analyzed by ion chromatography (IC) using two Methrom Eco-IC devices. TOC and total carbon (TC) were analyzed using TOC-L Shimadzu device. The TOC of the feedwater is (approximately) equal to the dissolved organic carbon (DOC). Total inorganic carbon (TIC) was determined by subtracting the TOC from the TC. TIC fractions (CO_2, HCO_3^-, and CO_3^{2-}) were determined depending on the pH. WTW 3310 and inoLab Cond 7310 (both Xylem Inc.) handheld devices were used to determine the pH and EC in addition to online measurements. Detailed information on the lab analysis can be found in the Supplementary Information chapter 1.1.

2.5. Calculations and estimation of measurement uncertainty

All displayed permeabilities represent corrected permeabilities (P_C), which apply correction functions for temperature and osmotic pressure. The flux (J_P) was corrected to 25 °C using a temperature correction function (TCF) from the membrane supplier [22]. To consider the osmotic pressure, the transmembrane osmotic pressure (TMπ) is subtracted from the transmembrane pressure (TMP). The TMπ is calculated based on a relation between electrical conductivity (EC) and osmotic pressure (π), as described in our previous study [24].

$$P_C = \frac{J_P{*}TCF_{25°C}}{TMP - TM\pi} \tag{1}$$

Recovery within CC-mode (ϕ_{CC}) is a function of the CC-time (t_{CC}), the system volume ($V_{Syst.}$), and the flux, i.e., the permeate flow (Q_P).

$$\phi_{CC} = \frac{Q_P{*}t_{CC}}{Q_F{*}t_{CC} + V_{Syst.}} = \frac{Q_P{*}t_{CC}}{Q_P{*}t_{CC} + V_{Syst.}} \tag{2}$$

The observed recovery ($\phi_{Obs.}$) can be determined by:

$$\phi_{Obs.} = \frac{Q_P}{Q_F} = \frac{Q_P}{Q_P + Q_B} \tag{3}$$

Since no brine is discharged in CC-mode, the observed recovery is 1, i.e., 100 %. The hydraulic concentration factor ($CF_{Hyd.}$) was calculated based on the CC-recovery (ϕ_{CC}) by Eq. (4).

$$CF_{Hyd.} = \frac{1}{1 - \phi_{CC}} \tag{4}$$

Moreover, the concentration factor of selected constituents (CF_X) was calculated by the ratio between the respective concentrations of concentrate ($c_{C,x}$) and feed ($c_{F,x}$). The hydraulic pressure loss (Δp) was determined by the difference between the feed (p_F) and concentrate pressure (p_C). Rejections refer to the bulk rejection of the selected constituents (Bulk Rej.), see Eq. (5). The recovery of a single pass is low ($Q_P/Q_{F,inner} < 0.1$), so the concentrations in the bulk ($c_{Bulk} = \frac{c_{F,inner}+c_C}{2}$) and concentrate ($c_C$) can be assumed to be approximately equal for simplification ($c_{Bulk} \approx c_C$). Furthermore, in Exp. 3.2, the apparent rejection was displayed for nitrate (NO_3^-) and hydrogen carbonate (HCO_3^-), see Fig. 4 e). The apparent rejection determined using the (outer) feed concentration (c_F) instead of the concentrate concentration (c_C). The different concentrations considered within the study are depicted in Fig. 1.

$$Bulk\ Rej. = 100\%{*}1 - \frac{c_P}{c_{Bulk}} \approx 100\%{*}1 - \frac{c_P}{c_C} \tag{5}$$

The salt passage (SP) was calculated based on the conductivity in the permeate (EC_P) and the concentrate (EC_C) with:

$$SP = 100\%{*}\frac{EC_P}{EC_C} \tag{6}$$

Data analysis was performed using Python 3 within a Jupyter Notebook environment; detailed information can be found in our previous study [24]. PhreeqC (Version 3.8.6.17100, released January 7, 2025) was used to calculate the saturation index (SI) of relevant mineral phases considering the ion activity product (IAP) and the respective solubility product (K_{SP}):

$$SI = log_{10}\frac{IAP}{K_{SP}} \tag{7}$$

The SI was calculated for both the feed and the concentrate. For the concentrate during CCRO operation, the calculation refers to the final concentration immediately before flushing is initiated. Moreover, the database was expanded to include selected precursors of calcite, namely vaterite and amorphous calcium carbonate (ACC), anhydrous and hydrated ACC, taking into account the respective solubility product and enthalpy of dissolution using the collected data from Rodriguez-Navarro et al. [43]. Detailed information is attached to the Supplement Information chapter 1.3.

The adjusted database was used to simulate flushing-induced dissolution of various calcium carbonate deposits. Since the dissolution increases the pH value and the concentration of dissolved calcium and TIC-species, the SI of the solutions in the simulation was adjusted to correspond to the experimentally determined pH increase. The equilibrium phases term was used to increase the SI stepwise until the simulation matched the experimental pH. Following the calculated increase of calcium and TIC, the results were compared with the experimental data. Since a recovery of approximately 10 % was achieved in flushing, the respective concentration factor was considered in addition to the increase due to dissolution. Therefore, the composition of the concentrate during flushing was simulated with WAVE (Version 1.83 Dupont) using the same membrane, flux, recovery, and feedwater as in the experiment.

The measurement uncertainty was calculated based on the combined standard uncertainty according to DIN ISO 11352, which considers the reproducibility and the systematic error [44]. Moreover, for calculations based on multiple measurements, e.g., the rejection and the concentration factor, the error propagation was considered using Gaussian error propagation of the combined standard uncertainty. Since the concentrations of the TIC-species, CO_2, HCO_3^-, and CO_3^{2-}, depend on the TIC and the pH measurement, respective error-propagations were applied for each species. All depicted errors (error bars and error surfaces) show the combined standard uncertainty or its propagation. Additionally, the plausibility of measurements was checked using PhreeqC, considering the ion balance of measured anions and cations. Moreover, the overall accuracy of both ions and flow rates was checked using mass balances and calculating the mass flow deviation ($\Delta\dot{m}$) based on the input (feed) and output (permeate + concentrate).

$$\Delta\dot{m} = \frac{\left(\dot{m}_{Perm.} + \dot{m}_{Conc.}\right) - \dot{m}_{Feed}}{\left(\dot{m}_{Perm.} + \dot{m}_{Conc.}\right)} = 1 - \frac{\dot{m}_{In}}{\left(\dot{m}_{Out}\right)} \tag{8}$$

The uncertainty calculations are described in detail in the Supplementary Information chapter 1.2, using Exp. 0 as an example for the error analysis.

3. Results and discussion

3.1. Evaluation of membrane performance parameters under non-scaling conditions

Fig. 2 a) and b) depict one CC run of Exp. 1 framed by previous and subsequent flushing-mode (grey boxes) in non-scaling conditions. In this

example, the CC-mode lasted 53 min, while the flushing duration was five minutes. The course of recovery and flux within a CC run is shown in Fig. 2 a). The CC-recovery ϕ_{CC} (squares) increases with time in CC-mode (t_{CC}) following a saturation function shape and reaches at the end of the CC-mode a recovery of approximately 84 %, representing a hydraulic concentration factor (CF) of 6.25. In the flushing mode, only a small portion of permeate is produced initially, as indicated by the rapid drop in flux and recovery. The targeted flux (25 LMH) is reached after approximately one minute (constant flux operation within CC-mode).

In Fig. 2 b) and c), the same excerpt of CC-mode is shown for the course of concentrate-EC and -pH. Due to the increasing recovery in CC-mode, the concentrate-EC increases roughly linearly with time due to the high rejection of ions, e.g., HCO_3^--rejection in Fig. 2 d. Moreover, the concentrate pH increases too, however, the growth is logarithmic, following the relation of the pK_{a1} and the concentrations of HCO_3^- and CO_2:

$$pH_{Conc.} \approx pK_{a1} + \log\left(\frac{[HCO_3^-]}{[CO_2]}\right) \quad (9)$$

The increase is therefore attributable to the high rejection of the alkalinity compounds HCO_3^- and CO_3^{2-}, see Fig. 2 d. The rejection of HCO_3^- approaches the hydraulic concentration factor (≈ 6), whereas CO_3^{2-} reaches a CF of roughly 9.3, exceeding the hydraulic CF, as the

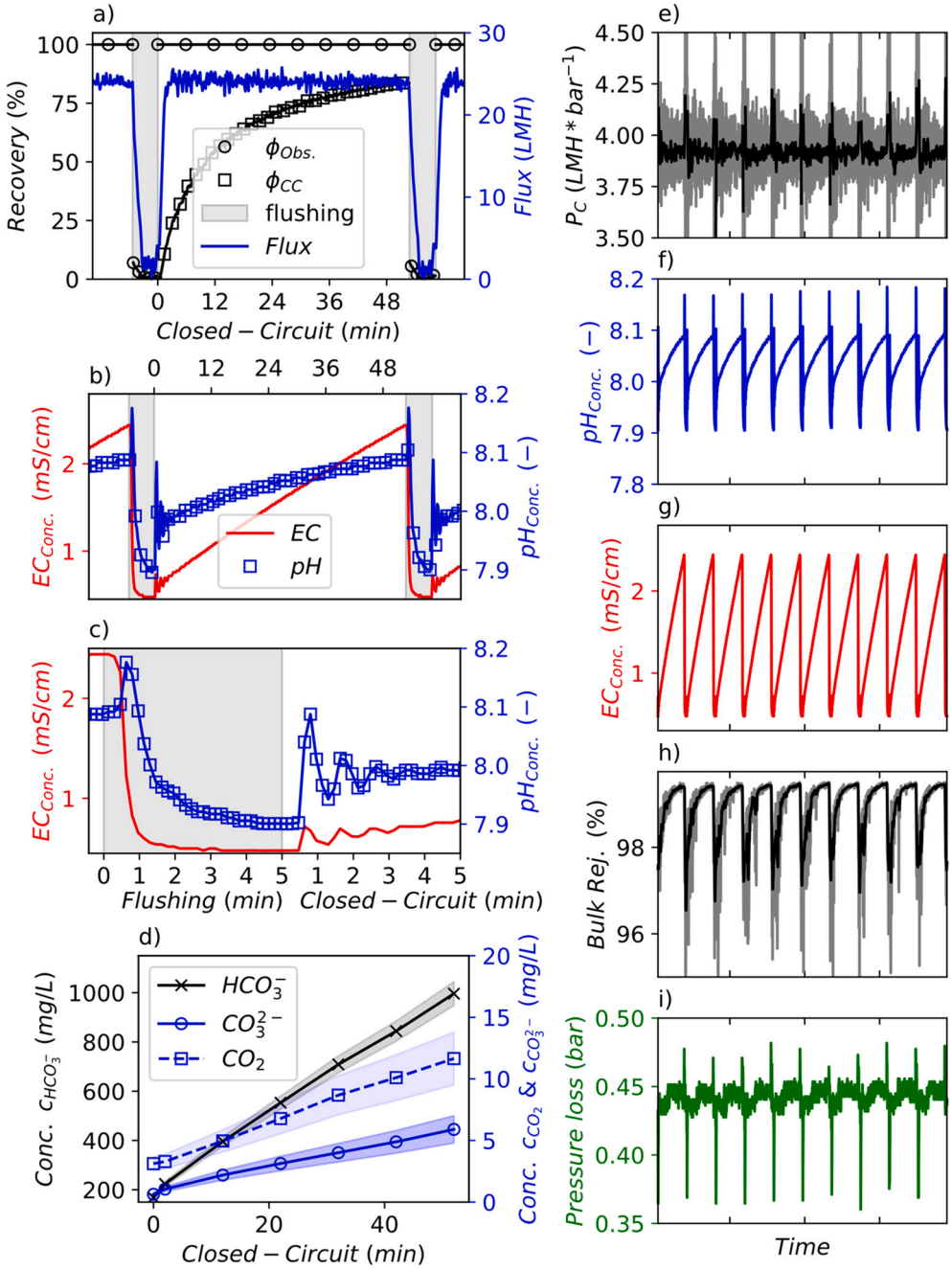

Fig. 2. Exp. 1 with BW30 at 25 LMH and 84 % recovery with detailed view of a CC-mode framed from previous and consecutive flushing (grey boxes) showing the recovery and flux (a) and the concentrate-EC and pH (b). c) Excerpted transition from flushing to CC-mode; d) Concentrate concentrations of inorganic carbon species in CC-mode. The transparent areas represent the combined standard uncertainty. Connecting the points is intended purely for visual guidance. e) to i) show the permeability, concentrate pH and -EC, bulk EC-rejection and pressure loss over the time for 10 consecutive cycles (the grey lines represent the raw data and the black lines, the moving average for the permeability and the rejection).

CO_3^{2-}proportion of the TIC increases with the pH value. Moreover, although dissolved gases, such as CO_2, are not retained by RO-membranes [22,45], the concentration of CO_2 also increases with time, i.e., recovery, see Fig. 2 d, but reaches a significantly lower CF (≈3.7). This increase is attributed to the increase of TIC, which approaches the hydraulic CF, too, since HCO_3^- is the major fraction of the TIC in this pH range. Although the relative fraction of CO_2 decreases due to the rise of pH from the feed (≈2.5 %) to the concentrate (≈1.6 %), the absolute amount of CO_2 concentration increases due to a roughly sixfold increase in the TIC from approximately 3 to 12 mg CO_2/L. Shortly after flushing, a damped oscillation is visible in the CC-mode for the concentrate EC and pH (Fig. 2 c). This fluctuation is caused by a quantity of concentrate located in a dead space (roughly 6 % of the system volume), which is not rinsed in the flushing mode and mixes with the rinsed volume and the incoming feedwater in the consecutive CC-mode. Approximately 6 % of the system volume (dead space) remains unrinsed during flushing. Moreover, due to non-ideal flushing that deviates from plug flow behavior, axial dispersion leads to a salt accumulation [20,46,47]. The oscillations arise from the interaction of convection and dispersion during the subsequent CC phase, when the unrinsed and rinsed fractions mix, coupled with the restart of permeation [1]. As dispersion diminishes with time, a steady linear increase in conductivity is established [1]. Fig. 2 c) also shows that within the first minute of flushing mode, the concentrate EC drops rapidly and, as expected, reaches the feed-EC value after a short time, as the recovery approaches zero. Unexpectedly, however, the pH value of the concentrate rises and reaches a peak value between half a minute and one minute after the start of flushing. In addition, it takes significantly longer for the concentrate pH value to reach the feed-pH value of approximately 7.9 than for the concentrate-EC value to reach the feed-EC of roughly 0.5 mS/cm.

Our hypothesis for the sharp pH increase of about 0.1 units and the elevated time to reach the feed-pH is that CO_2 degassing affects the carbonic acid equilibrium. When flushing is initiated, the applied pressure quickly approaches the atmospheric pressure, resulting in an almost complete cessation of permeate flux and recovery (Fig. 2 a) and potentially in CO_2 degassing, which could explain the temporary increase in concentrate pH in transition from CC- to flushing-mode (Fig. 2 c). The CO_2 concentration in the concentrate is almost 20 times higher (≈12 mg CO_2/L) than the equilibrium CO_2 concentration (≈0.65 mg CO_2/L with Henry constant $H_S^{cp} = 34.45$ mol / (m^3 * atm) at 25 °C [48] and 430 ppm of CO_2 in the atmosphere in June 2025 [49]). Since the main driving force for CO_2 degassing, i.e., the $CO_{2(g)}$-flux, is the concentration gradient between the actual and the equilibrium concentration, degassing is likely [50,51]. A simple calculation example for CO_2 degassing is provided in the Supplementary Information (chapter 2.1).

If this hypothesis is true, a solution with a neglectable quantity of dissolved CO_2 should not induce a pH-peak when the pressure is released, i.e., in the transition from CC- to flushing-mode. Fig. 3 a) and b) compare the transition from CC- to flushing-mode with two different feedwaters: a) tap water with dissolved CO_2 (pH_{Feed} ≈ 7.8 with ≈ 3.0–3.5 mg $CO_{2(aq)}$/L), and a synthetic water (b) containing 10 mM Na_2CO_3 (pH_{Feed} > 10.5 with ≈ 0.01 mg $CO_{2(aq)}$/L).

The tap water exhibits a pronounced concentrate pH peak in transition from CC- to flushing mode. In contrast, the concentrate pH of the Na_2CO_3 solution closely follows the EC curve, without any transient increase, thus supporting the hypothesis that CO_2 degassing is responsible for the observed pH peak. For both the Na_2CO_3 solution and the tap water, a permeate pH peak is observed during the transition, although it is more pronounced in the latter. The slight increase observed for the Na_2CO_3 solution can be attributed to the increasing salt passage resulting from the declining permeate flux (black line). Since dense membranes have (complete or partly) decoupled salt and water fluxes, increasing the water flux increases the dilution on the permeate side and

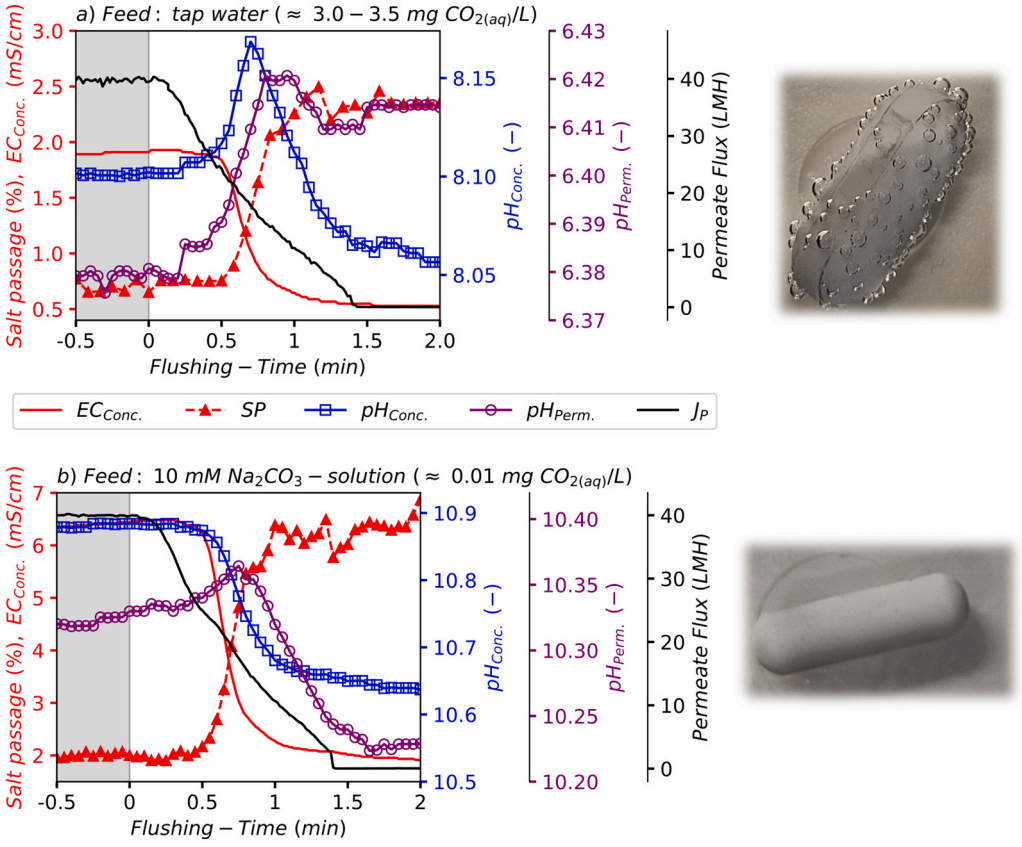

Fig. 3. Exp. 2 transition from CC-mode (grey box) to flushing for a) tap water and b) 10 mM Na_2CO_3-solution; Photographs show magnetic stirrers submerged in samples of tap water concentrate (top right) and 40 mM Na_2CO_3 solution (bottom right).

thus lowers the permeate concentration of retained compounds, i.e., higher rejection, see also Fig. 4 a to c. In contrast, for the tap water, it is the combination of increased salt passage and the elevated concentrate pH that synergistically leads to a more pronounced permeate pH peak. Another indication of CO_2 degassing is the formation of bubbles around the magnetic stirrer in a sample of tap water concentrate, whereas no bubble formation was observed in the Na_2CO_3 solutions (see Fig. 4 on the right). A video provided in the Supplementary Information illustrates the CO_2 degassing in a tap water concentrate sample. This mechanism of CO_2 release in the transition from CC- to flushing-mode has not yet been described in the literature. Possible cleaning benefits induced by those mechanisms are discussed in chapter 3.3.

Fig. 2 e) depicts the course of permeability, concentrate pH (f), and EC (g), the bulk-rejection (h), as well as the pressure loss (i) for 10 consecutive cycles. The constant progression of all five parameters indicates no scaling and negligible fouling conditions. The permeability does not exhibit a decreasing trend, and the concentrate pH and EC values repeatedly reach the same maximum at the end of a cycle. $CaCO_3$ precipitation, on the other hand, would be indicated initially by decreasing pH and EC in the concentrate and in a later state by decreasing permeability and rejection as well as by an increasing pressure loss [24].

Interestingly, in CC-mode, the bulk-EC rejection increases with time, see Fig. 2 h). Gu et al. [23] reported a slight increase of (bulk-) rejection (e.g., for TOC, EC, TDS) with CC-mode, too, however, the underlying reasons were not discussed. Compaction effects due to increasing pressure within the CC-mode are unlikely. On the one hand, the membrane was sufficiently compacted before the experiments, i.e., until a stable salt rejection and permeability was reached. On the other hand, the permeability did not decrease with time in CC-mode, as it would be expected due to compaction effects [52], i.e., compaction increases the rejection and decreases the permeability. However, compaction cannot be ruled out entirely, since insufficient permeability correction functions may overshadow the respective permeability decline. We, however, believe that the increase in bulk rejection is mainly connected to two mechanisms. The initial heavy increase is related to the time required to reach the targeted flux. Fig. 4 a) to c) depict the rejection and flux for the end of a CC-mode, flushing-mode, and the following CC-mode at 30, 10, and 20 LMH. When flushing is initiated (grey box), the rejection decreases (red downward arrow) since the flux decreases. In flushing-mode, the flux approaches quickly 0 LMH, i.e., no permeate flow, resulting in a constant EC reading (grey arrow). When the subsequent CC-mode starts, the flux increases. However, the rejection decreases (second red downward arrow). This is related to the hydraulic retention time in the permeate pipe. The decreasing rejection represents the rinse-out of that permeate, which was produced when the flux was decreasing to 0 LMH, and therefore has the lowest quality.

As soon as the poor-quality permeate is displaced, the rejection increases significantly (green upward arrow) almost in parallel with the flux, due to the dilution effect described earlier. However, even when the targeted flux is reached, the rejection, although at a lower rate, continues to increase (second green upward arrow). This increase is potentially connected to the increase of the concentrate pH with time in a CC-mode (see Fig. 2 b). Since dissolved gases, such as CO_2, cannot be retained by dense membranes [22,45], but all other carbonic acid species are largely retained, the concentrate pH value rises inherently during the process.

Fig. 4 d) shows that with the decreasing pH, the rejection decreases. By investigating the influence of pH on the rejection of selected water constituents, the positive correlation between pH and rejection becomes more apparent. Fig. 4 e) shows the moderate increase of nitrate (NO_3) rejection with the increasing pH. Nitrate was chosen because the rejection of other relevant ions (calcium, magnesium, sodium, sulfate) is significantly higher, resulting in permeate concentrations below the limit of quantification under the given condition of a low recovery. Chloride was excluded because it is added to the system via HCl dosing. A positive correlation of feed-pH and rejection of ions is documented in the literature [53–56], particularly for nitrate [57]. An increase in pH

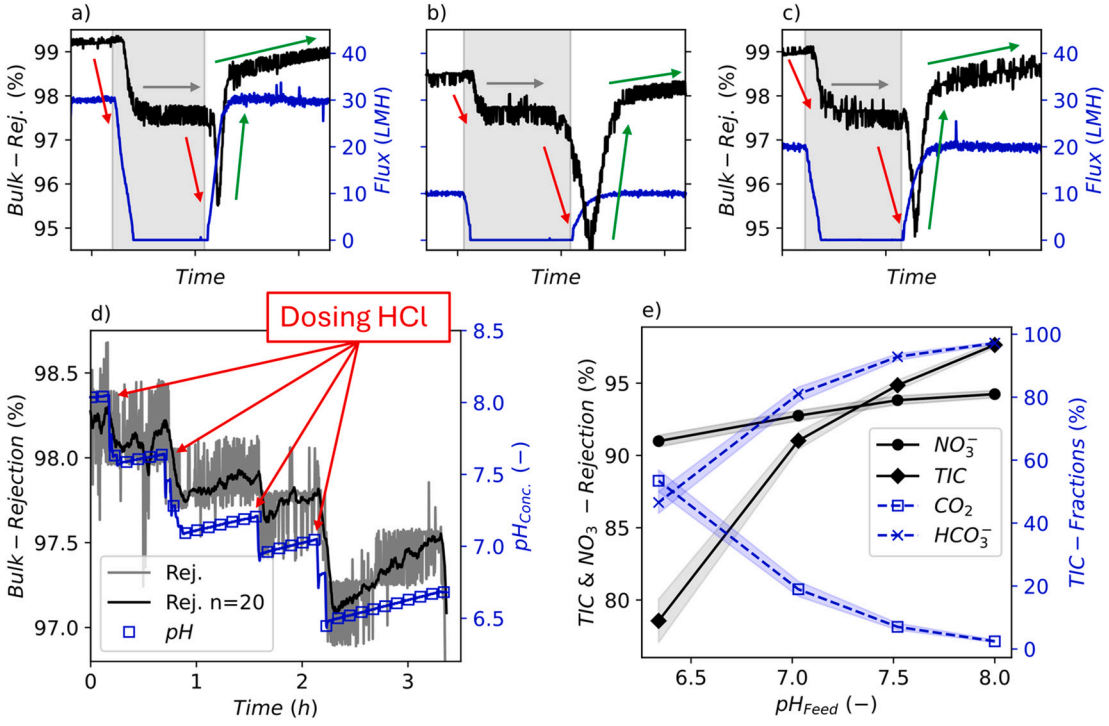

Fig. 4. Exp. 3.1 Transition from CC- to flushing- and to CC-mode for a water flux of (a) 30 LMH, (b) 10 LMH and (c) 20 LMH; d) Exp. 3.2 Bulk-EC and concentrate pH overtime with marked dosing points of HCl; e) Rejection of TIC; NO_3 and TIC-fractions depending on the feed-pH; The transparent areas represent the propagated error for the rejection and the minimum and maximum error for the TIC-fractions. Connecting the sampling points (dotted, solid lines and transparent areas) is intended purely for visual guidance.

leads to the deprotonation of the carboxylic functional groups of the membrane [53], thereby increasing the negative charges of the membrane (i.e., lowering the zeta-potential) [56,58]. The increasing negative charges increase the repulsion of anions (co-ions) and, to maintain electronegativity, of cations (contra-ions) [53], resulting in an overall higher rejection.

The TIC-rejection also shows an increase with increasing pH, but this increase is considerably more substantial, with roughly 20 % (Fig. 4 e). This can be explained by the influence of pH on the TIC species. With the increasing pH, the fraction of the charged TIC species increases, while the fraction of CO_2 declines. Thus, TIC-rejection decreases in the lower pH range, and both the shift towards charged TIC compounds and the increasing negative charge on the membrane with increasing pH value explain the significant increase in TIC-rejection. Since HCO_3^- is the dominant anion in the feedwater (see Table 1), the increase in the sum-parameter bulk-rejection based on the EC can be predominantly attributed to the increasing TIC rejection. A further example on the positive correlation between pH and rejection is given in Fig. S4 in the Supplementary Information.

The pH-influence also explains why the rejection further increases with higher flux, see Fig. 4 a) to c). The higher flux results in a higher recovery in CC-mode (constant CC-time), consequently in a higher concentration factor and thus a higher concentrate pH.

The relation of the inherently increasing pH with the cycle length in semi-batch and batch-operation could be further relevant in explaining the retention mechanism for charged micropollutants, e.g., for the (primarily) negatively charged poly- and perfluoroalkyl substances (PFAS). Recently, Masters et al. [59] reported an increase in the rejection of, e.g., highly charged PFOS with increasing recovery for the NF90 and argued, for instance, increased sorption with increasing recovery. However, as demonstrated in our study, one possible reason for this could be the increasing pH value with increasing recovery, which leads to higher charge repulsion.

In addition, this effect should be considered when implementing pretreatment strategies to mitigate the risk of $CaCO_3$ scaling, such as CO_2 dosing or acid ion exchange. These approaches can serve as alternatives to the use of antiscalants but may lead to a reduction in overall solute rejection due to the lower feed and thus concentrate pH.

3.2. $CaCO_3$-Scaling detection

In Exp. 4, scaling was provoked to investigate possibilities for its early detection. Therefore, the plant was operated at a constant flux of 25 LMH, and the recovery was increased stepwise by prolonging the CC-time, see Eq. (2). Fig. 5 a) depicts the permeability curve, where the horizontal arrows indicate increases in CC-recovery. The numbers one to four represent the points at which feed and concentrate samples were taken. The permeability was constant until 60 to 65 h, and then started to drop rapidly, indicating scaling. It took approximately 20 h after increasing the recovery to 87 %, until scaling was implied by declining permeability.

Scaling, i.e., precipitation, depends mainly on two conditions: thermodynamics, i.e., a certain supersaturation, and kinetics, e.g., induction time. Since each CC-mode reached the same maximum concentration ($SI_{Calcite} \approx 2.02$), i.e., had the same thermodynamics, and had the same length (65 min), i.e., the same kinetics, it is surprising that it took almost 20 cycles after the increase in recovery before scaling was indicated by the permeability. For once, this could be related to the random nature of nucleation [60], which could be translated to CCRO operation, where, with each CC-mode, with a certain probability, a critical nuclei formation can occur. Consequently, with an increasing number of cycles, the probability increases. On the other hand, the permeability might not be sensitive enough to indicate scaling, and other parameters, such as the concentrate pH, may detect scaling at a much earlier stage [24].

Fig. 5 b) depicts the ion concentration factor (CF_x) for Ca^{2+}, Mg^{2+}, SO_4^{2-} (left y-axis) and for CO_3^{2-} (right y-axis) for the sampling points.

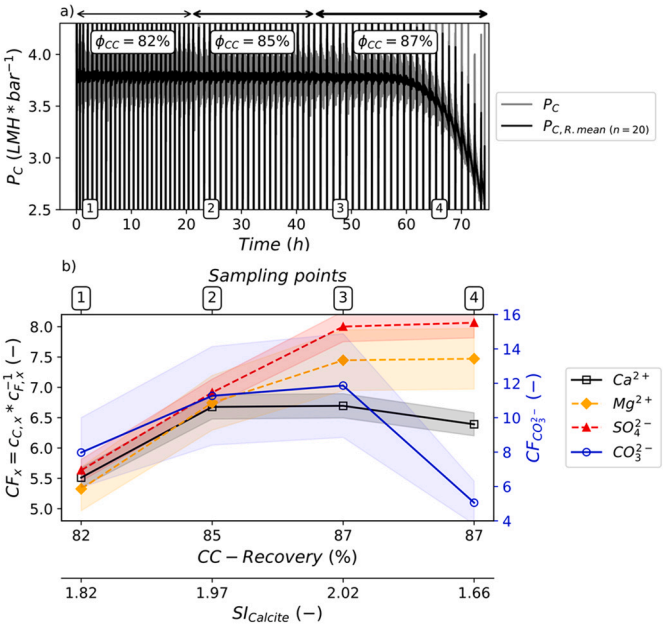

Fig. 5. Exp. 4 with BW30 at 25 LMH with stepwise increase of the recovery; a) permeability curve over time; numbers in lower boxes indicate sampling points, and the boxes below arrows indicate the respective recovery; b) Concentration factor (CF) of selected ions for each sampling point (top x-axis) with respective recovery and $SI_{Calcite}$ of the concentrate at the end of CC-mode (bottom x-axes); The transparent areas represent the deviation from the CF, calculated as the propagated combined standard uncertainty. Connecting the sampling points (dotted, solid lines, and transparent areas) is intended purely for visual guidance.

From sampling point 2 to 3 (85 and 87 % recovery), the CF of Ca^{2+} did, in contrast to Mg^{2+} and SO_4^{2-}, not further increase, and even decreased between sampling point 3 and 4, although the recovery was kept constant. For point 1 the CF for CO_3^{2-} (right y-axis) is the highest of all considered ions. This can be explained by the high rejection of negatively charged multivalent ions and the increasing pH with rising CF, which increases the fraction of CO_3^{2-}(see also Fig. 2 d). Both stagnation with increasing recovery and the decline with constant recovery of calcium and carbonate concentrations indicate $CaCO_3$ precipitation.

If the increase in calcium had followed the same trend from sampling point 2 to 3 as it did from point 1 to 2, the concentration would have reached roughly 580 mg/L instead of the measured 502 mg/L. However, since the permeability did not decline, we assume that reversible scaling and lowered rejection rates are responsible for the loss of almost 80 mg Ca^{2+}/L (representing 200 mg/L of $CaCO_3$). Alternating between CC- and flushing-mode could reversibly remove newly formed scale deposits.

Moreover, the accumulation of calcium ions at negatively charged functional groups of the membrane [61] could increase the calcium concentration at the membrane surface and consequently reduce the rejection. This initial accumulation could further lead to the formation of nucleation sites [61] with CO_3^{2-}/HCO_3^- for $CaCO_3$-formation, leading to the later experienced scaling.

Tracking the concentration of scaling-relevant ions could thus be a feasible tool to detect scaling at an early stage. For instance, the suspiciously low calcium concentration was sampled almost 15–20 h before declining permeability. However, ion determination of concentrate samples is elaborate, time-consuming, and necessitates sophisticated analytical tools. Moreover, sample preparation and running the analysis (in our case, ion chromatography) lead to a substantial delay between sampling and result generation. However, a possible option would be the integration of ion-selective electrodes (e.g., calcium) into the concentrate line for online measurement, which would necessitate further investment, frequent calibration, and replacement. Beyond that,

especially with $CaCO_3$ scaling, a simple pH measurement indirectly shows precipitation of $CaCO_3$ through an increase in protons, i.e., a decrease in the pH value, when $CaCO_3$ forms [24,62]. Therefore, further methods, in particular concentrate pH measurements, were investigated for their capability of early $CaCO_3$ scaling detection.

Fig. 6 gives a more detailed excerpt of shortly before and during the scaling event for permeability (a), bulk EC-rejection (b), concentrate EC (c), hydraulic pressure loss (d), and concentrate pH (e). As expected, $CaCO_3$ sacling impacted all five parameters, resulting in a decline of permeability, concentrate pH and EC, an increasing pressure loss, and a decrease in rejection [24], although the point in time of the respective changes varied. The yellow arrows indicate the point in time when the first signs of precipitation were observed in two consecutive cycles. The maximum EC in the concentrate at the end of a CC-mode was 3.05 mS/cm (dashed red line in Fig. 6 c). The yellow arrow thus points to the second consecutive cycle in which the maximum EC was not reached. The same concept applies to pressure loss and bulk rejection, all indicating first signs of scaling at roughly the same cycle. Permeability started to decline significantly later than all other parameters. Approximately three hours after the decrease in concentrate EC, pressure loss, and bulk rejection, the permeability declined slightly for the first time in two consecutive cycles. However, the suitability of using permeability for early detection in CCRO operation could be enhanced by employing a custom-made correction function for osmotic pressure, tailored to the specific feedwater composition, rather than, as in our case, relying on a standard function and by considering concentration polarization, e.g., following the suggested permeability correction of Benecke et al. [63]. The findings regarding concentrate EC are of practical significance with respect to CCRO control strategies. In general, there are three primary options for controlling the duration of the CC-mode: termination at a preset maximum pressure, at a maximum concentrate EC, or, as implemented in this study, by applying a defined time limit yielding in a constant hydraulic recovery (at constant flux operation). Using the concentrate-EC as a trigger point [23], carries thus the risk of amplifying the extend of a scaling-event, since the declining concentrate EC would be compensated by a longer CC duration further increasing the recovery and thus the saturation. Since EC-based control is typically implemented to respond to fluctuations in water composition [23], it is advisable to consider a defined factor of the feed water EC rather than the concentrate EC setpoint for this purpose.

The earliest warning was given by the concentrate pH (Fig. 6 e), which indicated precipitation approximately 6 h before the concentrate EC, pressure-loss, bulk-rejection, and roughly 10 h earlier than the permeability. Moreover, the warning signs of the concentrate pH were significantly amplified over time with each cycle, providing a clear and significant indication of $CaCO_3$ precipitation. This is in accordance with our previous study investigating $CaCO_3$ scaling in continuous RO operation, in which the concentrate pH was the earliest and most reliable indicator for incipient $CaCO_3$ scaling [24], and with another recent study [64] on $CaCO_3$ scaling, where the pH was the second fastest detection parameter after the calcium-concentration.

The initial warning signs of the concentrate pH are further illustrated in Fig. 6 f) to i), which depicts four complete cycles (CC-mode and subsequent flushing-mode) in non-scaling conditions (f), with first and moderate signs of $CaCO_3$-precipitiation (g and h), and with severe signs (i). All four examples precede the permeability drop. During non-scaling conditions, a similar trend as in Fig. 2 b) can be observed: The concentrate pH is rising continuously logarithmically within increasing CC-time. The first signs of $CaCO_3$ precipitation can be identified by flattening of the concentrate pH at elevated CC-times. Fig. 6 g) shows that the concentrate pH does not rise further in the last quarter of the CC-mode. The signs of $CaCO_3$ precipitation intensify when the concentrate pH starts to drop within a CC-mode. In Fig. 6 h), the concentrate pH peaks at about two-thirds of the CC-mode and then declines. The decrease becomes more pronounced in the following cycles, which significantly improves the accuracy of early warning. In Fig. 6 i), the

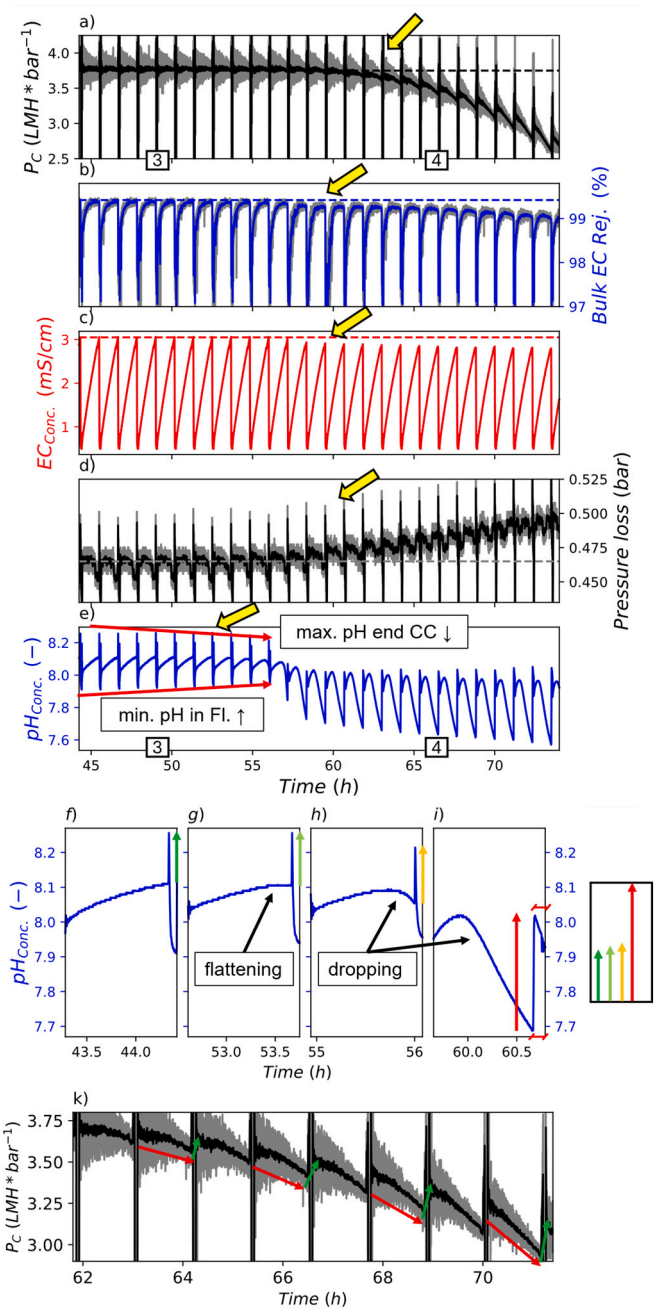

Fig. 6. Exp. 4 with detailed excerpt shortly before and within the scaling event for the permeability (a), concentrate pH and EC (b, c), hydraulic pressure loss (d) and bulk EC-rejection (e); black dashed line represents the average permeability before scaling; red dashed line depicts the maximum EC at the end of a CC-mode; grey dashed line is the average hydraulic pressure loss before scaling and blue dashed line is the maximum rejection before scaling; numbered boxes indicate point of feed and concentrate sampling.

maximum concentrate pH is already reached after one-third of the CC-mode, followed by a heavy decrease of approximately 0.3 pH units. Further data processing of concentrate pH measurements may improve detection sensitivity. Schwiebert et al. [25] calculated, for instance, the rate of turbidity change, to account for difference in the absolute feed turbidity among various feed waters. In the Supplementary Information (see Fig. S5), we included an example demonstrating how the temporal evolution of the pH difference could serve as a suitable indicator for further improvement in early detection. Additionally, it should be noted that the permeate pH provides a comparable capacity for early scaling

detection, closely mirroring the behavior of the (see Supplementary Information, Fig. S6).

Moreover, the temporary pH peak in transition from CC- to flushing-mode, which was linked under non-scaling conditions to CO_2 degassing (see chapter 3.1), increases. From Fig. 6 f) to i), the pH peak increased from 0.1 to 0.3 pH-units. In addition to the higher pH, the area under the curve increases, showing that the elevated pH persists for a higher flushing volume (Fig. 6 b).

We assume that the increase in the pH peak is related to the dissolution of $CaCO_3$ deposits formed in CC-mode and partially removed in flushing-mode. $CaCO_3$ dissolution leads to the consumption of protons and the release of HCO_3^-/CO_3^{2-}, causing the pH value to rise. This, in turn, could explain the increase in the pH in flushing mode (see red arrows pointing upwards in Fig. 6 e), because elevated $CaCO_3$ scaling in CC-mode leads to greater $CaCO_3$ dissolution during flushing, which in turn causes pH values to rise. This could also explain why the permeability drop is relatively moderate initially. With each flushing mode, the scaling layer is partially removed, leading to partial restoration of the permeability, see Fig. 6 k) with the green arrows indicating the permeability restoration.

3.3. *Feed flushing induced cleaning*

To prove the hypothesis of (partial) $CaCO_3$ dissolution under feed flushing conditions, Exp. 5 was conducted (see Fig. 7). Therefore, scaling was forced at elevated flux and CC-time (grey-box), and in flushing-mode, a low discharge flow rate (180 L/h) was chosen to allow extended sampling of the discharged concentrate. Fig. 7 a) depicts permeability, concentrate EC, and pH over time and the mass-flow deviation ($\Delta\dot{m}$) for selected constituents. In contrast to the previous experiments, the permeability decreased before the concentrate pH, which is explained later on in detail. Shortly before flushing, samples were taken from feed, permeate, and concentrate to determine whether constituents were accumulating on the membrane using a mass balance (see Fig. 7 a). Approximately 16 % of TIC and 23 % of calcium are lost from input (feed) to output (concentrate and permeate). In combination with the dropping concentrate pH, accumulation of $CaCO_3$ on the membrane is evident. Moreover, an accumulation of TOC is noticed (≈ -10 %), which indicates organic fouling [65–68]. Since the TOC of the feedwater consists of humic acids (HA), see chapter 2.1, HA-fouling is likely. Humic substances, e.g., HA, contain the two acidic functional groups carboxylic and phenolic hydroxyl, which deprotonate with increasing pH (first carboxylic-, above 8 phenolic-groups) [69]. Thus, the negative charges of HA increase with increasing pH, and consequently, reduced organic fouling by adhesion of HA onto the negatively charged membrane can be expected [67]. However, at elevated pH values, e.g., in concentrates, calcium ions chelate with deprotonated carboxylic acid groups [70], i.e., the negatively charged functional groups of organic polymers cross-link with divalent positively charged calcium, as has been described for alginate [71]. Thereby, calcium will reduce interchain repulsion and create a compact NOM layer [72], increasing organic fouling, e.g., for HA- [67], or alginate-fouling [68,73]. In general, the influence of organic matter on scaling is complex, and both milder and more severe permeability decline can occur. Mangal et al. [74] demonstrated that the presence of humic substances drastically increases the induction time of $CaCO_3$ precipitation, from less than 1 h to more than 7 days and suspected that adsorption of humic substances onto $CaCO_3$ growth sites hinders crystallization. A similar conclusion was reached by Benecke et al. [63], who reported antiscaling effects of various organic macromolecules, for instance HA, on gypsum formation. Overall, our results indicate the same antiscaling mechanism, as also reported in our previous study using the same water matrix [24], which presumably allows to reach high supersaturations (e.g., in Exp. 4 $SI_{Calcite} = 1.97$), without the occurrence of scaling. However, at higher recovery and flux, as in Exp. 5, we expect a different mechanism, which would further explain why the permeability declines first, followed by

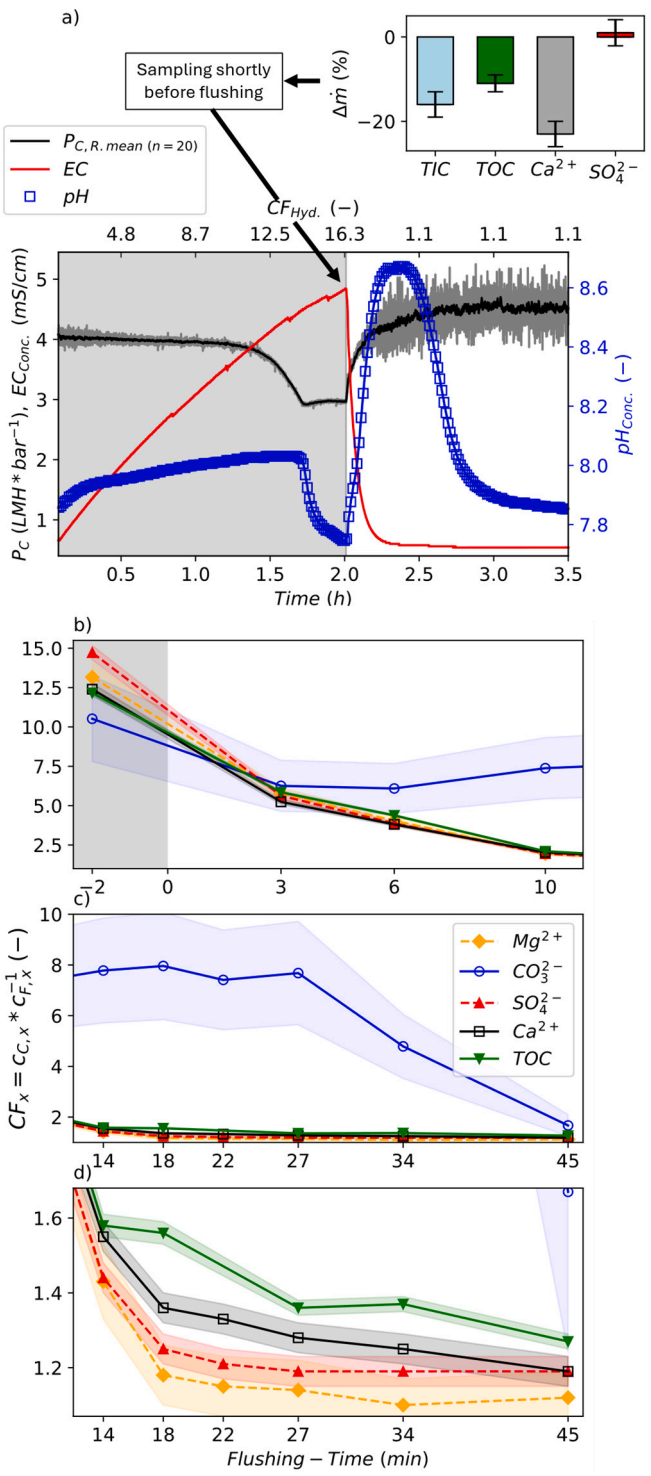

Fig. 7. Exp. 5 a) CC-mode (grey background) in transition to extended flushing for the permeability, concentrate-EC and pH over time. Right top depicts the mass balance shortly before flushing; b) to d) Concentration factor for different species over the flushing time at low discharge flow rate (180 L/h); c) and d) give the same time frame with different resolution for the concentration factor;

the concentrate pH. Malkoske et al. [66] showed severe permeability loss in the combination of HA fouling and $CaCO_3$ scaling and identified an organic fouling layer beneath the $CaCO_3$ crystals. Thus, indicating that the organic fouling layer deposits first, which can be further explained by the kinetics of $CaCO_3$ formation, which necessitates a certain induction time [24]. Interestingly, the permeability stopped to

decrease at the same time, when the pH started to drop, which was moreover reproduced, see Supplementary Information Fig. S8. A comparable behavior of the permeability was observed by Nnebuo et al. [75]. In their study, they step wise increased the concentration of $CaCl_2$ and $NaHCO_3$ to force $CaCO_3$ scaling. Initially, a sharp permeability decline was observed, followed by a temporary increase and subsequent plateauing of the permeability [75]. The initial decline was attributed to heterogeneous nucleation on the membrane, whereas the subsequent increase was linked to a transition to particulate fouling due to bulk precipitation [75]. The growth of larger particles, which are more susceptible to shear-induced diffusion and may be sheared off, further explains the permeability increase [75]. However heterogeneous nucleation is an unlikely explanation for the initial permeability loss observed in our study. Besides the lack of the concentrate pH response, there is also no effect on other scaling indicators. There is neither an increase in pressure loss nor a loss in rejection (see Supplementary Information Fig. S7), the latter of which was reported by Nnebuo et al. [75]. We believe that the temporal stabilization of the permeability is rather linked to precipitation in the concentration polarization layer, reducing the concentration directly at the membrane and thus increasing the permeability, as described in our previous study [24]. Therefore, we conclude that the initial permeability drop is presumably linked to organic fouling, however, more studies are necessary to investigate the complex interaction between fouling and scaling in CCRO operation. The flushing-mode led to a heavy increase of the concentrate pH, indicating for once the release of CO_2 due to pressure release as explained in chapter 3.1. This time, however, the increase was more significant (pH increase by more than one unit) and prolonged (the peak value was reached after approximately 30 min, while it took more than one hour to approach the pH value of the feed). Beyond that, permeability also increased when flushing began. For once, the permeability increase can be explained by the reduced flux (from 30 to 7 LMH), reducing concentration polarization. However, the flux is lowered quickly (seconds), while the permeability increases continuously, parallel to the concentrate pH. Thus, increased permeability and concentrate pH indicate dissolution of $CaCO_3$ deposits, reducing the hydraulic resistance.

Fig. 7 b) depicts the transition from CC-(grey-box) to flushing-mode. As expected, the CF of all constituents decreases with increasing flushing time. However, after three minutes, the carbonate-CF started to increase and was stable for more than 20 min at approximately eight, although all other parameters dropped already below two (Fig. 7 b). The CF of calcium was also noticeably higher for more than 20 min compared to the other investigated ions (Fig. 7 c). The combination of elevated carbonate and calcium concentrations in the flushing water, together with rising pH values and increasing permeability, supports the hypothesis of $CaCO_3$ dissolution due to flushing.

The dissolution of $CaCO_3$ under the given conditions is surprising, although dissolution is reported in literature, e.g., induced by flow-reversal [21,76]. However, these studies used an undersaturated feedwater, i.e., the ion activity product (IAP) undercuts the solubility product, and in this study, the feedwater was supersaturated with regard to the (under ambient conditions) thermodynamically most stable form, calcite [77,78]. Thus, calcite dissolution with the given feedwater is thermodynamically impossible, since the IAP exceeds the solubility product. However, in our previous study, we observed clear signs of $CaCO_3$ dissolution induced by forward flushing, too, using the same supersaturated water [24].

The explanation for this phenomenon is presumably that $CaCO_3$ precipitation involves multiple consecutive transformations from unstable to metastable and finally to the most stable phase [77,79,80], departing from classical crystal growth theory [78,81]. Ostwald's law of stages explains that: if a solution is supersaturated with multiple phases, the thermodynamically most stable phase is (usually) preceded by less stable phases [78–80]. Calcite has several precursors, i.e., unstable forms, such as polymer-induced liquid precursors, amorphous calcium carbonate (ACC) [78], e.g., hydrated and anhydrous ACC [43,82], and metastable polymorph crystalline forms such as aragonite and vaterite [43,77]. Since the precursor have a higher similarity to the surrounding aqueous environment than calcite, e.g., due to stronger hydration, the surface energy penalty due to the interfacial area between the forming nucleus and the solution [81] is lower, which leads to lower energy barriers for a stepwise transformation compared to a direct formation of metastable or stable phases [78]. The lower stability leads to higher solubility (higher K_{SP}) and consequently to a lower SI of the unstable compared to the stable phase (calcite) [43]. It is likely that within the short period of CC-mode, the thermodynamically less stable and lower saturated precursors of calcite precipitate, which dissolve in contact with feedwater, since their solubility is significantly higher than that of calcite. Recently, Malkoske et al. [66] identified various $CaCO_3$ forms in a fouling layer, consisting not only of calcite, but also of vaterite, aragonite, and ACC.

PhreeqC calculations using an extended database for $CaCO_3$ (vaterite, anhydrous and hydrated ACC, see chapter 2.5) revealed that in the feedwater, i.e., flushing-water, all less stable precursors are undersaturated, with SI values of −0.18, −1.09 and −2.06 for vaterite, anhydrous and hydrated ACC, respectively, compared to the more stable aragonite and calcite, with SI values of 0.25 and 0.39, respectively. This reveals that dissolution of precursors is thermodynamically possible in contrast to the stable forms. To further link the experimental observations of the release of TIC-species and calcium (Fig. 7 b to d), the dissolution of anhydrous ACC was simulated with PhreeqC. When $CaCO_3$ deposits dissolve, the pH value increases and the concentration of calcium and TIC in solution increases, which raises the SI. In the simulation, the SI was iterated (see chapter 2.5) until the measured pH was obtained. Fig. 8 a) depicts the measured experimental (left bars with error bars) and the simulated concentrations (left y-axis) as well as the deviation between experiment and simulation (right y-axis). Minimal deviations between the experiment and simulation were obtained for Ca^{2+}, Mg^{2+}, Na^{+}, SO_4^{2-}, and HCO_3^{-} (< 5 %). Although the simulation provides CO_3^{2-} values in the correct order of magnitude, the deviations are high (approx. 50 %), which is mainly due to the strong influence of small changes in pH and HCO_3^{-} concentration on the CO_3^{2-}concentration. If the slightly higher experimental HCO_3^{-} were used instead of the simulated value, the deviation for CO_3^{2-} would already be reduced by 35 %. Moreover, in this pH range, carbonate represents only about 2 % of the TIC-fractions. Therefore, small measurement uncertainties in pH measurement lead to high deviations of the calculated CO_3^{2-} concentration (see Supplementary Information chapter 1.2).

The simulation, thus, supports the theory that the permeability loss and pH drop in CC-mode are related to the precipitation of calcite precursors, e.g., ACC. Flushing with feedwater causes the precursors to dissolve, as they are undersaturated in the feedwater. This, in turn, leads to an increase in pH and permeability. Further studies should investigate the exact forms of $CaCO_3$ depostions, e.g., using Raman spectroscopy [43]. Beyond that, our studies suggest that the standard procedure for evaluating scaling potential based on parameters describing the thermodynamically most stable phase, calcite (e.g., $SI_{Calcite}$, Langelier Saturation Index – LSI), should be reconsidered for batch and semi-batch operation, as the thermodynamically less stable forms tend to precipitate within the short supersaturation times. Therefore, parameters considering amorphous precursors, e.g., Monohydrated LSI [83,84], are presumably more suitable. Our results, thus, extend the theory on salinity cycling in batch and semi-batch operation [13,14]: the short period at high saturation presumably fosters the formation of precursors rather than of stable forms. Further research should investigate whether amorphous forms also develop under conditions when antiscalants are dosed.

In our previous study [24], we found that after a certain time following a scaling event, forward flushing is no longer effective in restoring permeability. This is probably related to converting unstable precursors into more stable forms. We therefore consider timely forward

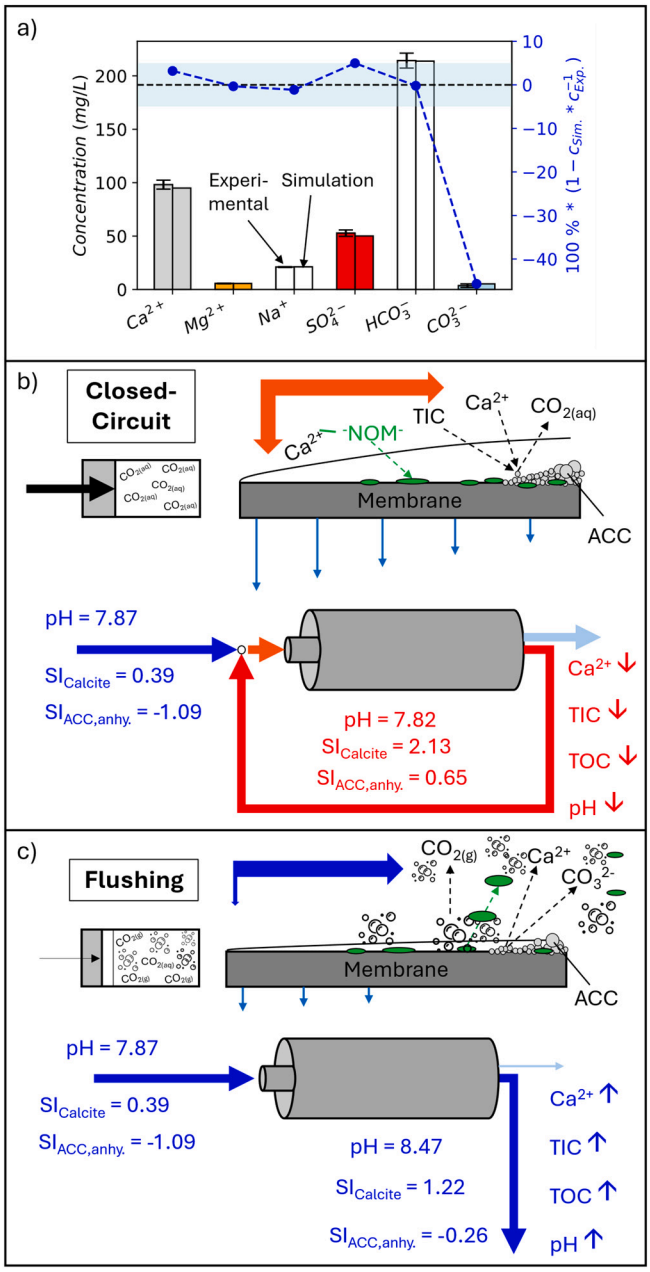

Fig. 8. Exp. 5 a) Comparison of experimental (left bars) with simulated (right bars) concentrations (left y-axis) and deviation of experimental from simulated values (right blue y-axis). Error bars display the combined standard uncertainty; Mechanism of scale formation in b) closed-circuit (the SI in the concentrate is determined at the end of the CC-mode) and c) dissolution in flushing-mode and.

flushing to be much more effective, as the precipitates formed mainly consist of unstable precursors that are undersaturated in the flushing water.

Moreover, the CF of the TOC is continuously elevated, even after 45 min of flushing (Fig. 7 d). Therefore, permeability recovery is presumably a combination of removing $CaCO_3$ deposits and the organic fouling layer. The removal of the organic fouling layer is surprising, too. Malkoske et al. [66] showed, for instance, that during continuous RO operation, combined organic fouling and $CaCO_3$ scaling leads to irreversible permeability loss, which could only be marginally restored physically. High-pressure RO operation leads to a compacted organic fouling layer, which typically cannot be removed physically, e.g., forward-flush [85]. Assuming that in our experiments the organic fouling layer is located beneath the inorganic scaling deposits, as in [66], the (partial) dissolution of the overlying inorganic deposits by flushing coupled with the reduction in hydraulic pressure and permeation drag force can lead to a decompaction of the fouling layer and possible detachment due to the increased shear-forces during flushing. In addition, due to the cyclic nature of CCRO operation, the frequent pressure release might lead to a less compacted or reversible organic-fouling layer. Moreover, the mechanism of CO_2 degassing due to the frequent pressure relief in the transition from CC-mode to flushing (see chapter 3.1) might further contribute to the permeability recovery. Alnajjar et al. [68] reported improved permeability restoration using CO_2 saturated solutions compared to conventional forward-flushing and suspected that a fouling layer acts as additional nucleation sites for CO_2 bubbles, thereby increasing bubble formation, which induces additional shear forces that remove the fouling layer [86]. However, further studies should investigate combined organic-fouling and inorganic scaling in CCRO operation in more detail. For instance, to clarify if the transition from CC- to flushing-mode yields in the formation of CO_2 bubbles, which contribute to removing fouling layers. Moreover, the pH increase might, besides physical means, chemically enhance the removal of an organic fouling layer. The increase can loosen the fouling layer by further dissociating the functional groups, thereby reducing their stability.

Fig. 8 b) shows the proposed formation mechanism of a combined anhydrous ACC and NOM layer in CC-mode, which manifests in a decrease in pH and TIC, TOC, and Ca^{2+} concentration, and the respective simulated SI-values in the concentrate. Dissolution of anhydrous ACC and removal of the NOM fouling layer, as well as the increase of pH, TIC, TOC, Ca^{2+}, and the respective SI-values, is depicted in Fig. 8 c).

Moreover, the mechanism of $CaCO_3$ dissolution and removal of the NOM-layer depicted in Fig. 8 c), serves as an explanation why they reached limiting recovery was significantly higher in the present CCRO study compared to our previous study, in which the same water-matrix and membranes were used but operated as continuous CoFRO [24]. In CCRO operation, both the flux (25 LMH) and the critical recovery (87 % with $SI_{Calcite} > 2.0$) were significantly higher compared to CoFRO operation, in which $CaCO_3$-scaling occurred repeatedly at 82.5 % ($SI_{Calcite} < 2.0$) and 20 LMH [24]. Further investigations are required before it can be concluded that CCRO is less susceptible to $CaCO_3$ scaling than continuous RO operation. Such research should not only consider the CC-recovery (see chapter 2.5) but also include unproductive flushing in order to make the overall recovery and flux comparable.

However, our findings suggest advantages of CCRO operation, in which flushing leads to dissolution of $CaCO_3$ deposits and organic fouling layers accompanied by temporal permeability recovery, see Fig. 6 k and increased concentration of fouling constituents in the flushing water, see Fig. 7 b) to d).

3.4. $CaCO_3$-Scaling mitigation by early scaling detection

Fig. 9 a) depicts a long-term experiment (more than 54 days) to investigate the feasibility of applying early $CaCO_3$ scaling detection by monitoring the concentrate pH. In this experiment, the flux was kept constant (36.5 LMH) while the CC-recovery was varied. The blue dashed lines represent a decrease in recovery compared to the previous operation, and the red dashed lines represent an increase. The recovery was adjusted by changing the time for a CC-mode, e.g., increasing the time to increase the recovery, see eq. (2).

The experiment started with an initial recovery of 87.5 % to force scaling. After approximately 20 h, the first signs of $CaCO_3$ precipitation were evident from the concentrate pH. Fig. 9 b) and c) show a close-up just before and after the point where the recovery was reduced (blue dashed line) and show the course of permeability and concentrate pH. As explained in chapter 3.2, the concentrate pH responded much earlier, as can be seen from the evaluation of the course of the subsequent CC-modes, which reached a lower final pH value, flattened out, and finally decreased during a cycle.

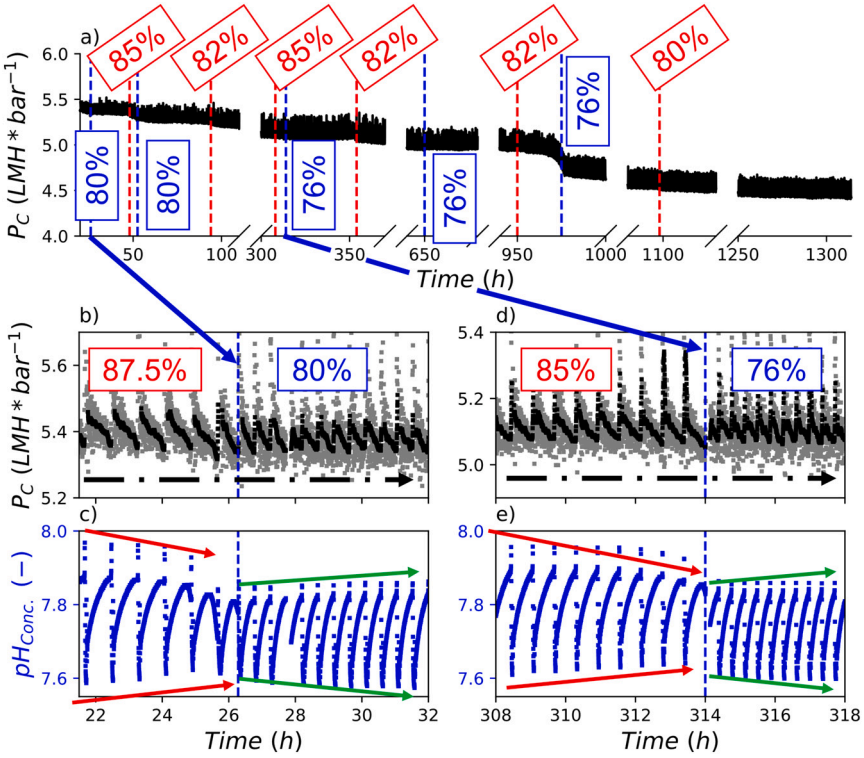

Fig. 9. Exp. 6: Constant flux (36.6 LMH) at varying recoveries (78 to 87.5 %) covering a bulk concentrate $SI_{Calcite}$ (end of CC-mode) of roughly 1.45 to 2.08. Blue dashed lines represent a decrease in recovery, red dashed lines indicate an increase in recovery; a) Permeability curve over time; b), c) and d), e) Excerpts on the permeability and concentrate pH from spots where the recovery was reduced in response to a suspicious concentrate pH signal.

Furthermore, the pH peak value decreases with each cycle during the transition to flushing, while the starting pH value of each cycle increases, indicating the removal and dissolution of $CaCO_3$ deposits. At the same time, the permeability showed no decreasing tendency (see Fig. 9 b). After lowering the recovery, the concentrate pH stopped declining and stabilized. The maximum and minimum concentrate pH increased and decreased with each cycle (green arrows (Fig. 9 c), indicating that several cycles with lower recovery were required until excess $CaCO_3$ deposits were dissolved, see also Supplementary Information Fig. S11 b. Fig. 9 d) and e) give a similar example with a recovery decrease from 85 to 76 % after early warning signs as indicated by the concentrate pH monitoring (Fig. 9 d), while permeability indicated no scaling (Fig. 9 e). A similar trend can be observed in this example, showing that the concentrate pH indicates $CaCO_3$ scaling early enough for countermeasures to be taken (blue dashed line).

Since the plant operated stably at a recovery of 76 %, the recovery was increased to 82 % after about 350 h of operation, see Fig. 9 a). The plant could be operated for a further 300 h without any signs of scaling. However, a slight permeability decline (0.09 %/d) was noticed, presumably related to organic fouling and potentially biofouling. Thus, the recovery was reduced to 76 % after 650 h, which reduced the decline to 0.03 %/d (see Supplementary Information Fig. S9). Thereafter, the plant ran stably for another 300 h before the recovery was increased again to 82 %. Although the plant had previously run stably for roughly 300 h at the recovery of 82 %, this time a decrease in the concentrate pH indicated $CaCO_3$ scaling (see Supplementary Information Fig. S11 b). Since the countermeasures were conducted with a certain time delay, e.g., in the examples in Fig. 9 b) and d), approximately four to six hours after the first signs from the concentrate pH, it is likely that some crystals were not removed from the membrane. These crystals probably act as nuclei, lowering the induction time at formerly stable saturation, explaining the decrease in the critical recovery. Although the concentrate pH again indicated $CaCO_3$ scaling before a drop in permeability was observed, the permeability started to decline earlier, presumably due to already existing crystal deposits on the membrane (see Supplementary Information Fig. S11 a). In contrast to the previous examples, where the focus was on preventing $CaCO_3$ scaling through early detection, this time, it was tested whether lowering the recovery could stabilize the system even after a substantial indication of scaling over a longer period. Although within 10 h the permeability declined by 17.5 %/d, lowering the recovery immediately stopped the heavy decrease to a moderate decline of roughly 1 %/d (see Supplementary Information Fig. S9 c). Furthermore, permeability stabilized further over time, reaching a decline of roughly 0.2 %/d, with no signs of $CaCO_3$ scaling. This once again underlines the advantages of the inherent process of flushing. In addition, an overall constant hydraulic pressure loss and salt rejection were observed throughout the entire test period (see Supplementary Information Fig. S12). Exp. 6 showcases that controlling the plant using the concentrate pH enables antiscalant-free desalination in CCRO operation, comparable to our previous study for CoFRO operation [24].

4. Conclusion

This study investigates CCRO operation without antiscalants dosage on a semi-technical scale using a real water matrix that induces $CaCO_3$ scaling. The aim of the study is to gain a deeper understanding of how its discontinuous operation affects membrane-performance, the detection of the onset of scaling, and the mechanisms for preventing scaling. Key findings include:

- Under non-scaling conditions, increasing the closed-circuit (CC) time and thus recovery leads to higher bulk rejection. This is accompanied by a rise in pH, which increases the fraction of charged, well-retained TIC species and enhances membrane surface charge, thereby strengthening charge repulsion.
- The concentrate pH provides the earliest indication of incipient $CaCO_3$ scaling, initially observed as a flattening of the typically

logarithmic increase in pH and, under stronger scaling, as a decline in concentrate pH.
- Long-time experiments under conditions close to $CaCO_3$ scaling without antiscalant confirmed the suitability of concentrate pH monitoring in combating scaling.
- Inherent process flushing with feed water (partially) dissolves $CaCO_3$ deposits, evidenced by increased concentrate pH, permeability, and higher TIC and Ca^{2+} concentrations in the discharged flushing water. This dissolution is likely promoted by short residence times at high saturation, favoring formation of amorphous, less stable precursors instead of calcite.
- Flushing also contributes to the removal of organic fouling, probably because cyclic pressure relief in CCRO produces a less compacted fouling layer.
- Transitioning from CC to flushing mode may induce CO_2 degassing, potentially aiding cleaning - a hypothesis warranting further study.

Overall, this study demonstrates anti-fouling and anti-scaling mechanisms inherent to CCRO, resulting in partial restoration of permeability even under severe scaling conditions. However, to fully assess the practical advantages of CCRO relative to conventional operation, a fair comparison must consider the required higher recovery and flux in CC modes, which offset the lower productivity during flushing phases.

CRediT authorship contribution statement

Martin Futterlieb: Writing – review & editing, Writing – original draft, Visualization, Validation, Supervision, Software, Project administration, Methodology, Investigation, Formal analysis, Data curation, Conceptualization. **Stefan Panglisch:** Writing – review & editing, Validation, Supervision, Resources, Project administration, Conceptualization.

Declaration of Generative AI and AI-assisted technologies in the writing process

The authors' original draft was edited with Grammarly Premium and Perplexity Pro to improve grammar, expression, and readability. Moreover, Perplexity Pro was used for troubleshooting in data processing using Python. After using these tools, the authors reviewed and edited the content as needed and took full responsibility for the publication's content.

Declaration of competing interest

The authors declare that they have no known competing financial interests or personal relationships that could have appeared to influence the work reported in this paper.

Acknowledgments

This research was partly conducted in the framework of the project KonTriSol (https://kontrisol.de/) and MAMDIWAS (https://www.uni-due.de/zwu/mamdiwas.php). The project KonTriSol was funded (grant no. 02WAV1530C) by the Federal Ministry of Education and Research of Germany (BMBF) and co-financed by the German Technical and Scientific Association for Gas and Water (DVGW). The project MAMDIWAS is funded (grant no. 02WAS1719A) by the BMFTR (Federal Ministry of Research, Technology and Space). The 2.5" plant was partially funded within the framework of "Innovative Wassertechnologie im FutureWaterCampus (InnoWat) by the European Regional Development Fund (ERDF) - EFRE-NRW 2014–2020 Program. We are thankful for the membrane supply from DuPont. The authors acknowledge the experimental contributions of Puneet Naresh Manghnani. We also gratefully acknowledge Prof. Dr.-Ing. Gerhard Braun (TH Köln) for emphasizing, during the International Symposium on Aminophosphonates and the Environment at BTU Cottbus, that calcite dissolution is thermodynamically not possible under the given water matrix conditions. This prompted us to re-examine the data set and to reproduce our results, which consistently repeated our initial results – a clear $CaCO_3$ dissolution. Ultimately, this led us to recognize that the observed dissolution is in fact related to amorphous precursors rather than calcite. We finally thank the anonymous reviewers for their helpful comments and suggestions that contributed to improving this manuscript.

Appendix A. Supplementary data

Supplementary data to this article can be found online at https://doi.org/10.1016/j.desal.2025.119622.

Data availability

Data will be made available on request.

References

[1] M. Li, Cyclic simulation and energy assessment of closed-circuit RO (CCRO) of brackish water, Desalination 545 (2023) 116149, https://doi.org/10.1016/j.desal.2022.116149.
[2] M. Li, Y. Heng, J. Luo, Batch reverse osmosis: a new research direction in water desalination, Sci. Bull. 65 (2020) 1705–1708, https://doi.org/10.1016/j.scib.2020.05.032.
[3] A. Efraty, R.N. Barak, Z. Gal, Closed circuit desalination — a new low energy high recovery technology without energy recovery, Desalin. Water Treat. 31 (2011) 95–101, https://doi.org/10.5004/dwt.2011.2402.
[4] P.A. Davies, Comparison of semi-batch reverse osmosis configurations, Desalination 608 (2025) 118805, https://doi.org/10.1016/j.desal.2025.118805.
[5] DuPont, DuPont to acquire desalitech, 20th of July 2025; Available from: https://www.investors.dupont.com/news-and-media/press-release-details/2019/DuPont-to-Acquire-Desalitech/default.aspx, 2019.
[6] S. Lin, M. Elimelech, Staged reverse osmosis operation: configurations, energy efficiency, and application potential, Desalination 366 (2015) 9–14, https://doi.org/10.1016/j.desal.2015.02.043.
[7] T. Qiu, P.A. Davies, Comparison of Configurations for High-Recovery Inland Desalination Systems: Water, 2012, pp. 690–706.
[8] D.M. Warsinger, E.W. Tow, K.G. Nayar, L.A. Maswadeh, J.H. Lienhard V, Energy efficiency of batch and semi-batch (CCRO) reverse osmosis desalination, Water Res. 106 (2016) 272–282, https://doi.org/10.1016/j.watres.2016.09.029.
[9] M. Futterlieb, I.M.A. ElSherbiny, M. Tuczinski, J. Lipnizki, S. Panglisch, Limits of high recovery inland desalination: closed-circuit reverse osmosis – a viable option? Chem. Ing. Tech. 93 (2021) 1359–1368, https://doi.org/10.1002/cite.202100042.
[10] S. Lin, M. Elimelech, Kinetics and energetics trade-off in reverse osmosis desalination with different configurations, Desalination 401 (2017) 42–52, https://doi.org/10.1016/j.desal.2016.09.008.
[11] J.R. Werber, A. Deshmukh, M. Elimelech, Can batch or semi-batch processes save energy in reverse-osmosis desalination? Desalination 402 (2017) 109–122, https://doi.org/10.1016/j.desal.2016.09.028.
[12] V. Sonera, J. Septon, A. Efraty, CCD series no-21: illustration of high recovery (93.8 %) of a silica containing (57 ppm) source by a powerful technology of volume reduction prospects, Desalin. Water Treat. 57 (2016) 20228–20236, https://doi.org/10.1080/19443994.2015.1126412.
[13] D.M. Warsinger, E.W. Tow, L.A. Maswadeh, G.B. Connors, J. Swaminathan, J. H. Lienhard V, Inorganic fouling mitigation by salinity cycling in batch reverse osmosis, Water Res. 137 (2018) 384–394, https://doi.org/10.1016/j.watres.2018.01.060.
[14] E. Hosseinipour, E. Harris, H.A. El Nazer, Y.M.A. Mohamed, P.A. Davies, Desalination by batch reverse osmosis (RO) of brackish groundwater containing sparingly soluble salts, Desalination 566 (2023), https://doi.org/10.1016/j.desal.2023.116875.
[15] E.W. Tow, Q.J. Wei, A.R. Abraham, K.L. Chua, M.J. Plumley, J.H. Lienhard, Piloting batch reverse osmosis with a flexible bladder for water recovery from scaling-prone brine, npj Clean Water 8 (2025) 30, https://doi.org/10.1038/s41545-025-00462-6.
[16] S.A. Kaushik, D. Armbruster, J. Dittmer, D. Bruniecka-Sulewski, B. Wendler, M. Ernst, Investigation of scaling inhibition and biofouling potential of different molecular weight fractions of a PAA antiscalant, npj Clean Water 7 (2024) 36, https://doi.org/10.1038/s41545-024-00332-7.
[17] M. Feiner, S. Beggel, N. Jaeger, J. Geist, Increased RO concentrate toxicity following application of antiscalants - acute toxicity tests with the amphipods *Gammarus pulex* and *Gammarus roeseli*, Environ. Pollut. 197 (2015) 309–312, https://doi.org/10.1016/j.envpol.2014.11.021.
[18] R. Kuhn, C. Vornholt, V. Preuss, I.M. Bryant, M. Martienssen, Aminophosphonates in nanofiltration and reverse osmosis permeates, Membranes-Basel 11 (2021), https://doi.org/10.3390/membranes11060446.

[19] D. Armbruster, U. Müller, O. Happel, Characterization of phosphonate-based antiscalants used in drinking water treatment plants by anion-exchange chromatography coupled to electrospray ionization time-of-flight mass spectrometry and inductively coupled plasma mass spectrometry, J. Chromatogr. A 1601 (2019) 189–204, https://doi.org/10.1016/j.chroma.2019.05.014.
[20] T. Lee, J.Y. Choi, Y. Cohen, Gypsum scaling propensity in semi-batch RO (SBRO) and steady-state RO with partial recycle (SSRO-PR), J. Membr. Sci. 588 (2019) 117106, https://doi.org/10.1016/j.memsci.2019.05.030.
[21] N. Pomerantz, Y. Ladizhansky, E. Korin, M. Waisman, N. Daltrophe, J. Gilron, Prevention of scaling of reverse osmosis membranes by "zeroing" the elapsed nucleation time. Part I. Calcium sulfate, Ind. Eng. Chem. Res. 45 (2006) 2008–2016, https://doi.org/10.1021/ie051040k.
[22] DuPont, FilmTec™ Reverse Osmosis Membranes Technical Manual, 2024.
[23] H. Gu, M.H. Plumlee, M. Boyd, M. Hwang, J.C. Lozier, Operational optimization of closed-circuit reverse osmosis (CCRO) pilot to recover concentrate at an advanced water purification facility for potable reuse, Desalination 518 (2021), https://doi.org/10.1016/j.desal.2021.115300.
[24] M. Futterlieb, S. Panglisch, Incipient CaCO3-scaling detection for scaling mitigation, Desalination 613 (2025) 119023, https://doi.org/10.1016/j.desal.2025.119023.
[25] A.M. Schwiebert, J.A. Bush, A. Bray, I. Reyes, A. Cortijo, H. Portilla, P. García-Chevesich, C. Bellona, T.Y. Cath, J. Vanneste, Turbidity-based scaling detection system for batch reverse osmosis combined with gypsum crystal recovery, Desalination 586 (2024) 117817, https://doi.org/10.1016/j.desal.2024.117817.
[26] S. Hager, H. Oesinghaus, A. Bachmann, M. Meinardus, T. Hofmann, R. Engelbrecht, K. Glas, CaCO3 deposits in reverse osmosis: Part III – Incipient Scaling detection via polymer optical fibre sensors. Comparison to hydrochemical prediction and image analytical methods, BrewingScience 76 (2023) 19–29, https://doi.org/10.23763/BrSc23-03hager.
[27] M. Uchymiak, A. Rahardianto, E. Lyster, J. Glater, Y. Cohen, A novel RO ex situ scale observation detector (EXSOD) for mineral scale characterization and early detection, J. Membr. Sci. 291 (2007) 86–95, https://doi.org/10.1016/j.memsci.2006.12.038.
[28] M. Uchymiak, A.R. Bartman, N. Daltrophe, M. Weissman, J. Gilron, P. D. Christofides, W.J. Kaiser, Y. Cohen, Brackish water reverse osmosis (BWRO) operation in feed flow reversal mode using an ex situ scale observation detector (EXSOD), J. Membr. Sci. 341 (2009) 60–66, https://doi.org/10.1016/j.memsci.2009.05.039.
[29] A.R. Bartman, E. Lyster, R. Rallo, P.D. Christofides, Y. Cohen, Mineral scale monitoring for reverse osmosis desalination via real-time membrane surface image analysis, Desalination 273 (2011) 64–71, https://doi.org/10.1016/j.desal.2010.10.021.
[30] H. Gu, A.R. Bartman, M. Uchymiak, P.D. Christofides, Y. Cohen, Self-adaptive feed flow reversal operation of reverse osmosis desalination, Desalination 308 (2013) 63–72, https://doi.org/10.1016/j.desal.2012.07.041.
[31] T. Lee, J.Y. Choi, Y. Cohen, Gypsum scaling propensity in semi-batch RO (SBRO) and steady-state RO with partial recycle (SSRO-PR), J. Membr. Sci. (2019), https://doi.org/10.1016/j.memsci.2019.05.030.
[32] J. Thompson, A. Rahardianto, S. Kim, M. Bilal, R. Breckenridge, Y. Cohen, Real-time direct detection of silica scaling on RO membranes, J. Membr. Sci. 528 (2017) 346–358, https://doi.org/10.1016/j.memsci.2017.01.027.
[33] O.D. Supekar, D.J. Park, A.R. Greenberg, J.T. Gopinath, V.M. Bright, Real-time detection of early-stage calcium sulfate and calcium carbonate scaling using Raman spectroscopy, J. Membr. Sci. 596 (2020), https://doi.org/10.1016/j.memsci.2019.117603.
[34] O.D. Supekar, J.J. Brown, A.R. Greenberg, J.T. Gopinath, V.M. Bright, Real-time detection of reverse-osmosis membrane scaling via raman spectroscopy, Ind. Eng. Chem. Res. 57 (2018) 16021–16026, https://doi.org/10.1021/acs.iecr.8b01272.
[35] D.J. Park, O.D. Supekar, A.R. Greenberg, J.T. Gopinath, V.M. Bright, Real-time monitoring of calcium sulfate scale removal from RO desalination membranes using Raman spectroscopy, Desalination 497 (2021) 114736, https://doi.org/10.1016/j.desal.2020.114736.
[36] D.J. Park, O.D. Supekar, V.M. Bright, A.R. Greenberg, J.T. Gopinath, Raman spectroscopy for real-time concurrent detection of multiple scalants on RO membranes, Desalination 565 (2023), https://doi.org/10.1016/j.desal.2023.116851.
[37] D.J. Park, O.D. Supekar, A.R. Greenberg, J.T. Gopinath, V.M. Bright, In-situ monitoring of calcium carbonate scale progression on reverse osmosis membranes using Raman spectroscopy, Desalin. Water Treat. 273 (2022) 92–103, https://doi.org/10.5004/dwt.2022.28883.
[38] W. Stumm, J.J. Morgan, Aquatic Chemistry, 3rd ed., 1996.
[39] Stadtwerke Duisburg, Chemisch - physikalische Wasseranalyse, 11th of March 2025; Available from: https://www.stadtwerke-duisburg.de/fileadmin/user_upload/Veroeffentlichungen/Trinkwasseranalyse_Nord.pdf, 2025.
[40] J.K. Edzwald, J.E. Tobiason, Enhanced coagulation: US requirements and a broader view, Water Sci Technol 40 (1999) 63–70, https://doi.org/10.1016/S0273-1223(99)00641-1.
[41] DuPont, FilmTec™ BW30 PRO-4040 & BW30 PRO-2540, 26th of September 2024; Available from: https://www.dupont.com/content/dam/dupont/amer/us/en/water-solutions/public/documents/en/RO-FilmTec-BW30-PRO-4040-and-BW30-PRO-2540-PDS-45-D03970-en.pdf, 2024.
[42] DuPont, FilmTec™ XLE PRO-4040 & XLE PRO-2540, 26th of September 2024; Available from: https://www.dupont.com/content/dam/dupont/amer/us/en/water-solutions/public/documents/en/RO-FilmTec-XLE-PRO-4040-and-XLE-PRO-2540-PDS-45-D03972-en.pdf, 2024.
[43] C. Rodriguez-Navarro, K. Kudłacz, Ö. Cizer, E. Ruiz-Agudo, Formation of amorphous calcium carbonate and its transformation into mesostructured calcite, CrystEngComm 17 (2015) 58–72, https://doi.org/10.1039/C4CE01562B.
[44] DIN, DIN ISO 11352:2013-03 - Wasserbeschaffenheit - Abschätzung der Messunsicherheit beruhend auf Validierungs- und Kontrolldaten (ISO 11352: 2012), 2013.
[45] S. Panglisch, M. Futterlieb, Membranverfahren - Grundlagen und Praxisanwendung, in: R. Winzenbacher, S. Panglisch (Eds.), Wasseraufbereitung - Grundlagen und Verfahren, Vulkan Verlag, 2025.
[46] Q.J. Wei, C.I. Tucker, P.J. Wu, A.M. Trueworthy, E.W. Tow, J.H. Lienhard, Impact of salt retention on true batch reverse osmosis energy consumption: experiments and model validation, Desalination 479 (2020) 114177, https://doi.org/10.1016/j.desal.2019.114177.
[47] T.Y. Qiu, P.A. Davies, Longitudinal dispersion in spiral wound RO modules and its effect on the performance of batch mode RO operations, Desalination 288 (2012) 1–7, https://doi.org/10.1016/j.desal.2011.11.054.
[48] R. Sander, Henry's Law Constants, 31th of July 2025; Available from: https://henrys-law.org/henry/casrn/124-38-9, 2025.
[49] NASA, Carbon Dioxide, 31th of July 2025; Available from: https://climate.nasa.gov/vital-signs/carbon-dioxide/?intent=121, 2025.
[50] L. Guo, L. Fang, P. Li, Y. Ma, Mass transfer of CO_2 gas pocket in horizontal pipe flow, Aqua - Water Infrastruct. Ecosyst. Soc. 73 (2024) 1164–1174, https://doi.org/10.2166/aqua.2024.326.
[51] R.O. Hall Jr., A.J. Ulseth, Gas exchange in streams and rivers, WIREs Water 7 (2020) e1391, https://doi.org/10.1002/wat2.1391.
[52] C.G. Patel, M. Joshi, J. Swaminathan, Membrane compaction in batch reverse osmosis operation and its impact on specific energy consumption, Desalination 592 (2024) 118132, https://doi.org/10.1016/j.desal.2024.118132.
[53] E.M. Kimani, M. Pranić, S. Porada, A.J.B. Kemperman, I.I. Ryzhkov, W.G.J. van der Meer, P.M. Biesheuvel, The influence of feedwater pH on membrane charge ionization and ion rejection by reverse osmosis: an experimental and theoretical study, J. Membr. Sci. 660 (2022) 120800, https://doi.org/10.1016/j.memsci.2022.120800.
[54] O. Coronell, B. Mi, B.J. Mariñas, D.G. Cahill, Modeling the effect of charge density in the active layers of reverse osmosis and nanofiltration membranes on the rejection of arsenic(III) and potassium iodide, Environ. Sci. Technol. 47 (2013) 420–428, https://doi.org/10.1021/es302850p.
[55] R. Epsztein, E. Shaulsky, N. Dizge, D.M. Warsinger, M. Elimelech, Role of ionic charge density in donnan exclusion of monovalent anions by nanofiltration, Environ. Sci. Technol. 52 (2018) 4108–4116, https://doi.org/10.1021/acs.est.7b06400.
[56] K.L. Tu, L.D. Nghiem, A.R. Chivas, Coupling effects of feed solution pH and ionic strength on the rejection of boron by NF/RO membranes, Chem. Eng. J. 168 (2011) 700–706, https://doi.org/10.1016/j.cej.2011.01.101.
[57] I. Koyuncu, Effect of operating conditions on the separation of ammonium and nitrate ions with nanofiltration and reverse osmosis membranes, J. Environ. Sci. Health A 37 (2002) 1347–1359, https://doi.org/10.1081/Ese-120005991.
[58] A.E. Childress, M. Elimelech, Effect of solution chemistry on the surface charge of polymeric reverse osmosis and nanofiltration membranes, J. Membr. Sci. 119 (1996) 253–268, https://doi.org/10.1016/0376-7388(96)00127-5.
[59] N.A. Masters, B.A. Marron, A. Lau, W.G. Bailey, S.D. Richardson, C.L. Bellona, Investigation of PFAS rejection by closed-circuit reverse osmosis and nanofiltration and sorption to treatment materials during groundwater treatment: a pilot demonstration, Sep. Purif. Technol. 377 (2025) 134308, https://doi.org/10.1016/j.seppur.2025.134308.
[60] S. Toschev, A. Milchev, S. Stoyanov, On some probabilistic aspects of the nucleation process, J. Cryst. Growth 13–14 (1972) 123–127, https://doi.org/10.1016/0022-0248(72)90073-5.
[61] Z. Steiner, H. Rapaport, Y. Oren, R. Kasher, Effect of surface-exposed chemical groups on calcium-phosphate mineralization in water-treatment systems, Environ. Sci. Technol. 44 (2010) 7937–7943, https://doi.org/10.1021/es101773t.
[62] T. Waly, M.D. Kennedy, G.J. Witkamp, G. Amy, J.C. Schippers, The role of inorganic ions in the calcium carbonate scaling of seawater reverse osmosis systems, Desalination 284 (2012) 279–287, https://doi.org/10.1016/j.desal.2011.09.012.
[63] J. Benecke, J. Rozova, M. Ernst, Anti-scale effects of select organic macromolecules on gypsum bulk and surface crystallization during reverse osmosis desalination, Sep. Purif. Technol. 198 (2018) 68–78, https://doi.org/10.1016/j.seppur.2016.11.068.
[64] M. Ait Mohand Said, K.-E. Bouhidel, Inhibition of calcium carbonate scaling in reverse osmosis by Zn^{++} using pure calco-carbonic solutions and the membrane CO_2 degassing method, Desalin. Water Treat. 321 (2025) 100952, https://doi.org/10.1016/j.dwt.2024.100952.
[65] C.S. Nnebuo, O. Nir, Backwashable hollow-fiber membranes enable ultrahigh recovery ratio effluent nanofiltration, Sep. Purif. Technol. 372 (2025) 133354, https://doi.org/10.1016/j.seppur.2025.133354.
[66] T.A. Malkoske, Y.-H. Cai, S.E. Bone, A.I. Schäfer, Calcium-organic matter fouling in nanofiltration: synchrotron-based X-ray fluorescence and absorption near-edge structure spectroscopy for speciation, Water Res. 272 (2025) 122938, https://doi.org/10.1016/j.watres.2024.122938.
[67] Y.-H. Cai, A. Gopalakrishnan, K.P. Deshmukh, A.I. Schäfer, Renewable energy powered membrane technology: implications of adhesive interaction between membrane and organic matter on spontaneous osmotic backwash cleaning, Water Res. 221 (2022) 118752, https://doi.org/10.1016/j.watres.2022.118752.
[68] H. Alnajjar, A. Tabatabai, A. Alpatova, T. Leiknes, N. Ghaffour, Organic fouling control in reverse osmosis (RO) by effective membrane cleaning using saturated

CO2 solution, Sep. Purif. Technol. 264 (2021) 118410, https://doi.org/10.1016/j.seppur.2021.118410.
[69] M.R. Collins, G.L. Amy, C. Steelink, Molecular weight distribution, carboxylic acidity, and humic substances content of aquatic organic matter: implications for removal during water treatment, Environ. Sci. Technol. 20 (1986) 1028–1032, https://doi.org/10.1021/es00152a011.
[70] M.Y. Abubasha, T.P.P. Le, J.K. Ali, A. AlFantazi, M.S. Jouini, D.L. Sanchez, E. Alhseinat, Real-time monitoring of organic fouling in reverse osmosis under hydrodynamic conditions: a comprehensive analysis, Desalination 599 (2025) 118463, https://doi.org/10.1016/j.desal.2024.118463.
[71] S. Lee, M. Elimelech, Salt cleaning of organic-fouled reverse osmosis membranes, Water Res. 41 (2007) 1134–1142, https://doi.org/10.1016/j.watres.2006.11.043.
[72] S. Hong, M. Elimelech, Chemical and physical aspects of natural organic matter (NOM) fouling of nanofiltration membranes, J. Membr. Sci. 132 (1997) 159–181, https://doi.org/10.1016/S0376-7388(97)00060-4.
[73] S. Lee, M. Elimelech, Relating organic fouling of reverse osmosis membranes to intermolecular adhesion forces, Environ. Sci. Technol. 40 (2006) 980–987, https://doi.org/10.1021/es051825h.
[74] M.N. Mangal, S.G. Salinas-Rodriguez, B. Blankert, V.A. Yangali-Quintanilla, J. C. Schippers, W.G.J. van der Meer, M.D. Kennedy, Role of phosphate and humic substances in controlling calcium carbonate scaling in a groundwater reverse osmosis system, J. Environ. Chem. Eng. 9 (2021), https://doi.org/10.1016/j.jece.2021.105651.
[75] C.S. Nnebuo, D. Hambsch, O. Nir, Elucidating morphological effects in membrane mineral fouling using real-time particle imaging and impedance spectroscopy, Environ. Sci.: Water Res. Technol. 8 (2022) 1444–1457, https://doi.org/10.1039/D2EW00155A.
[76] Y.A. Jarma, Y. Kim, Y. Cohen, Reverse osmosis desalination combining feed flow reversal with permeate flush for mitigation of mineral scaling, Desalination 574 (2024) 117273, https://doi.org/10.1016/j.desal.2023.117273.
[77] T. Ogino, T. Suzuki, K. Sawada, The formation and transformation mechanism of calcium carbonate in water, Geochim. Cosmochim. Acta 51 (1987) 2757–2767, https://doi.org/10.1016/0016-7037(87)90155-4.
[78] L.B. Gower, Biomimetic model systems for investigating the amorphous precursor pathway and its role in biomineralization, Chem. Rev. 108 (2008) 4551–4627, https://doi.org/10.1021/cr800443h.
[79] O. Söhnel, J. Garside, Precipitation: Basic Principles and Industrial Applications, 1992.
[80] I.V. Markov, Crystal Growth for Beginners: Fundamentals of Nucleation, Crystal Growth and Epitaxy, 1995.
[81] J. Rolf, T.C. Cao, X.C. Huang, C. Boo, Q.L. Li, M. Elimelech, Inorganic scaling in membrane desalination: models, mechanisms, and characterization methods, Environ. Sci. Technol. 56 (2022) 7484–7511, https://doi.org/10.1021/acs.est.2c01858.
[82] H. Nebel, M. Neumann, C. Mayer, M. Epple, On the structure of amorphous calcium carbonate—a detailed study by solid-state NMR spectroscopy, Inorg. Chem. 47 (2008) 7874–7879, https://doi.org/10.1021/ic8007409.
[83] H. Elfil, A. Hannachi, Reconsidering water scaling tendency assessment, AICHE J. 52 (2006) 3583–3591, https://doi.org/10.1002/aic.10965.
[84] S. Hager, A. Bachmann, T. Hofmann, R. Engelbrecht, K. Glas, CaCO3 deposits in reverse osmosis Part I – Shortcomings of current approaches leading to a new prediction model and monitoring device, BrewingScience 74 (2021) 122–133, https://doi.org/10.23763/BrSc21-12hager.
[85] M. Xie, J. Lee, L.D. Nghiem, M. Elimelech, Role of pressure in organic fouling in forward osmosis and reverse osmosis, J. Membr. Sci. 493 (2015) 748–754, https://doi.org/10.1016/j.memsci.2015.07.033.
[86] B. Jung, K. Park, Y. Kim, S. Han, S. Kim, D. Park, J. Soo Choi, Y. Yoon, S. Im, S. Lee, Using supercritical CO2 for alginate-fouled seawater reverse osmosis cleaning and for carbonate mineral production from concentrated brine, Sep. Purif. Technol. 354 (2025) 128627, https://doi.org/10.1016/j.seppur.2024.128627.